J. Fluid Mech. (2022), *vol*. 946, A17, doi:10.1017/jfm.2022.568

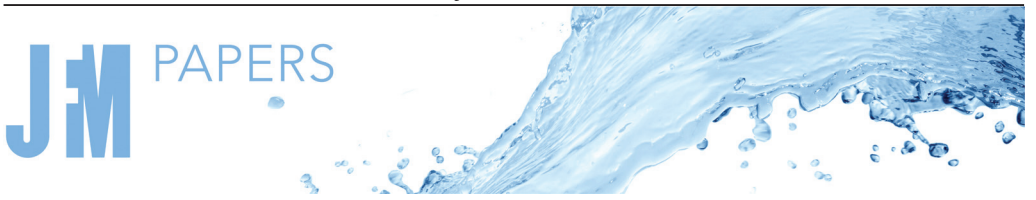

Natural convection in vertical enclosures with conjugate boundary conditions

Tomas Solano[1], **Juan C. Ordonez**[1] **and Kourosh Shoele**[1],†

[1]Department of Mechanical Engineering, Joint College of Engineering, Florida A&M University-Florida State University, Tallahassee, FL 32310, USA

(Received 12 October 2021; revised 10 May 2022; accepted 23 June 2022)

A numerical investigation and reduced-order modelling of natural convection in a cavity with differentially heated sidewalls is discussed. The effect of conjugate boundary conditions on the cavity's heat transfer and natural flow circulation with varying aspect ratios and Rayleigh numbers is examined. Validation of the canonical differentially heated cavity reveals that a modification to the definition of the Rayleigh number (Ra) is required to reconcile the $Nu \sim Ra^{1/4}$ scaling (where Nu is the Nusselt number) and validity of previously proposed correlations for the heat transfer in vertical enclosures. Dynamic mode decomposition is used to uncover the underlying time-dependent flow structures and the results are compared with stability bifurcation studies in the literature. A flow mode previously associated with smaller aspect ratio cavities is identified as the unstable mode for a larger aspect ratio of 4. The effect of conjugate boundary conditions is scaled based on the ratio of the internal and external boundary layers, wherein higher external Reynolds numbers aid in the heat transfer as the Nusselt number approaches the isothermal limit. A reduced-order theoretical model is proposed to predict the Nusselt number for the conjugate boundary conditions. The performance of conjugate boundary conditions is connected to the flow stability, with the parallel-flow configuration acting in a destabilizing manner while the counterflow configuration has a stabilizing effect and results in the highest heat transfer. We also found that relatively large heat transfer can be achieved with substantially lower external actuation with intermediate aspect ratios, translating to less power in practice.

Key words: buoyancy-driven instability, convection in cavities, buoyant boundary layers

1. Introduction

Buoyancy-driven flows appear in many applications, from atmospheric science to thermal management of power electronics. Natural convection flows in enclosures are of particular interest and can be subdivided into enclosures heated from the bottom and enclosures

† Email address for correspondence: kshoele@fsu.edu

heated from the side boundaries. The enclosure set-up is ubiquitous in many engineering systems such as insulation and ventilation of buildings (Ganguli, Pandit & Joshi 2009; Yang, Pilet & Ordonez 2018), heat exchangers (Kays & Alexander 1998; Yang & Ordonez 2019), thermal management of electronic devices and nuclear reactors (Azzoune *et al.* 2010) and the design of thermal storage tanks and solar thermal collectors (Buchberg, Catton & Edwards 1976).

In their most basic canonical forms, the above-mentioned systems can be represented as a rectangular enclosure with sidewall heating, also known as a differentially heated cavity (DHC) problem. Although the problem is simple in definition, its associated flow and thermal physics are complex. This is perhaps why this problem is frequently selected as a model problem. Moreover, due to the complex interaction of the core and boundary layers (Ostrach 1972; Bejan 2013), the DHC is considered a fundamental problem for studying flow-induced heat transfer. DHCs have been studied previously, starting with the pioneering work of Batchelor (1954), and the seminal works of De Vahl Davis (1983), which produced benchmark solutions for the numerical studies to come. Later, higher Rayleigh numbers and the transition to turbulent flow were investigated with computational models (Le Quéré 1991; Wan, Patnaik & Wei 2001).

Le Quéré (1990) showed that a steady-state flow solution can be obtained below a critical Rayleigh number (Ra_c), defined later in (2.4). However, beyond this critical point, the system undergoes the transition to time-dependent flow and eventually becomes turbulent. Specifically for air-filled cavities with aspect ratios ranging from 1 to 10, there has been much progress identifying the critical bifurcation points and stability of the system through the works of Christon, Gresho & Sutton (2002), Paolucci & Chenoweth (1989) and Xin & Le Quéré (2006) to name a few. Xin & Le Quéré (2006) studied instability mechanisms at small aspect ratios (less than 3) with adiabatic horizontal walls, small aspect ratios with conducting horizontal walls and large aspect ratios (larger than 3) independent of horizontal wall conditions. For small aspect ratios and adiabatic horizontal wall conditions, the instability was attributed to the 'hydraulic jump' at the corners downstream of the vertical boundary layers. The instability in small aspect ratio cavities with conducting horizontal walls was associated with the instability in the horizontal boundary layers, and for the large aspect ratios, the instability was observed as a travelling wave disturbance in the vertical boundary layers. In this paper, we only focus on enclosures with adiabatic horizontal top and bottom walls.

The boundary conditions of these problems can also trigger different paths of transition to turbulence and, consequently, modify the system's heat transfer. Such effects have been studied extensively in the related problem of Rayleigh–Bénard convection. The possibility of controlling the flow in Rayleigh–Bénard convection by perturbation of the thermal boundary conditions has been explored by Howle (1997). Abourida, Hasnaoui & Douamna (1999) showed that the system's overall heat transfer could be enhanced or reduced by proper choices of the time-variable heating modes at the top and bottom boundaries. Other studies have modified the Rayleigh–Bénard cells in a horizontal fluid layer with heating from the top and bottom using spatially sinusoidal boundary conditions (Asgarian, Hossain & Floryan 2016; Floryan, Shadman & Hossain 2018), wherein a higher heat transfer rate is observed for specific phase differences between the top and bottom boundary conditions. Similarly, for vertical enclosures with differentially heated sidewalls, the flow and thermal performance have been modified mechanically by vibrating boundaries or with the inclusion of rigid and flexible fins (Yucel & Turkoglu 1998; Xu 2006; Lappa 2016).

Thermal disturbances of the boundaries can induce significant changes to the systems' flow and heat transfer. It is shown that there exist special resonance conditions in a DHC

with fluctuating boundary conditions (Lage & Bejan 1993; Kwak, Kuwahara & Hyun 1998), where the heat transfer can be enhanced as a result of dynamic thermal disturbance on the boundary conditions near the DHC's inherent natural frequency. Kwak & Hyun (1996) imposed a time-varying temperature on an isothermal wall and observed that the highest overall heat transfer is achieved at the resonant frequency by varying the amplitude and frequency of the thermal boundary condition. Experimentally, Penot, Skurtys & Saury (2010) also studied the effect of a time-dependent disturbance at the resonant frequency of the cavity. Although an enhancement in heat transfer was expected, a 10 % reduction was observed. This was attributed to the disturbance mechanism, a protruding tube at the wall, which obstructed the flow. Turan, Poole & Chakraborty (2012) studied the effects of constant wall temperature and constant heat flux boundary conditions and found the heat transfer monotonically increases with the aspect ratio until a certain asymptotic value. In contrast, the maximum heat transfer occurs at a particular aspect ratio with the constant temperature boundary conditions. Recent studies by Chorin, Moreau & Saury (2018) and Thiers, Gers & Skurtys (2020) explored the use of a localized thermal disturbance on a vertical wall to trigger time-dependent flow with unsteady disturbances in an otherwise stable system to enhance the heat transfer.

By and large, the boundary conditions play a major role in the heat transfer and flow dynamics of DHCs. Although the system's heat transfer is expected to be optimal when the boundaries are held at a constant temperature, this condition is hardly possible in practice and if it could be achieved, it would be energetically expensive. More often, boundary heating or cooling is achieved through an external flow. However, to the best of our knowledge, there is no reported research on the effect of conjugate heat transfer boundary conditions on vertical enclosures. The configurations discussed here are similar to those typically employed in heat exchangers, particularly parallel and counterflow channel and shell-tube heat exchangers. It has been shown that the counterflow configuration leads to more effective heat transfer when compared with a parallel-flow configuration (Kakac, Liu & Pramuanjaroenkij 2002; Shah & Sekulic 2003; Çengel *et al.* 2008). However, it is still unknown how the heating or cooling of cavity boundaries with the external flow affects an enclosure's natural convection and its overall heat transfer. In the present investigation, we explore this aspect and study the effect of forced convection heating/cooling of the boundaries of a DHC on thermal performance and flow stability. Building on previous research on constant temperature boundaries, the basis for a 'unifying' theory of the heat transfer in these systems is extended here to derive appropriate scaling laws for heat transfer and instability mechanisms. We highlight the differences in the heat transfer with different configurations of externally heated/cooled vertical wall boundary conditions and connect these changes to the dominant flow dynamics caused by the boundary conditions. The instability mechanisms are investigated and an analytical model based on the boundary-layer solution will be proposed to predict the thermal performance of the conjugate boundary conditions. The analytical model then identifies the scaling laws governing heat transfer.

The rest of the paper is structured as follows: the problem is defined, along with a description of the models and numerical implementation, in § 2. In § 3, we compare the current model with results available in the literature and discuss the effect of the conjugate boundary conditions for different aspect ratios, Rayleigh numbers and external flow configurations. This section also discusses the effects of the conjugate boundary conditions on the time-dependent flow structures via modal analysis. Finally, we summarize our findings and discuss potential future directions in the last section.

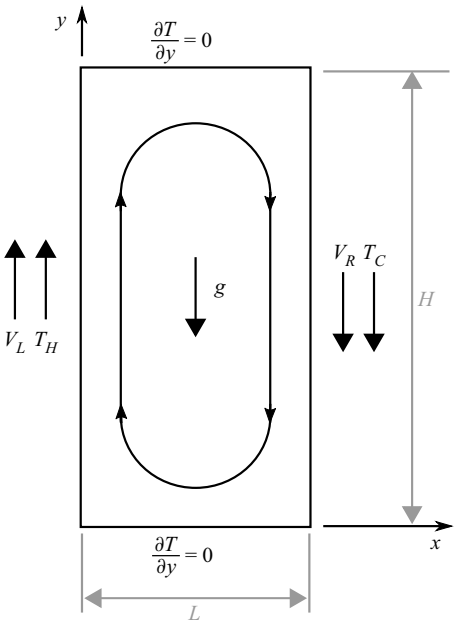

Figure 1. Schematic of a two-dimensional vertical enclosure differentially heated by external flows.

2. Problem definition

Here, a two-dimensional vertical rectangular cavity with adiabatic top and bottom walls, and differentially heated vertical sidewalls is considered as shown in figure 1. The aspect ratio (AR) is defined as the ratio of height (H) to width (L), $AR = H/L$. Gravity is along the $-y$ axis and the vertical walls are exposed to external forced convection. External heating/cooling with free-stream temperatures T_H and T_C, and free-stream velocities V_L and V_R are imposed on the left and right walls, respectively. The velocity and direction of the external forced convection are explored by varying the Reynolds number, $Re = VH\nu^{-1}$ (where ν is the kinematic viscosity of the fluid), and flow direction on either side of the DHC. The specific external flow configurations studied here are defined by flow direction at the left and right walls. Additionally, the cases of isothermal boundary conditions are included for comparison.

The system consists of an internal flow region governed by the buoyancy-driven circulation inside the enclosure and an external flow region governed by the wall-bounded external flow. Internal and external flow models are formulated independently and coupled at the vertical wall interface; thus, we call the external flow a conjugate boundary condition (CBC) for the DHC. The internal flow region is governed by the incompressible Navier–Stokes equations of continuity, momentum and energy with the Boussinesq approximation. With the use of the characteristic buoyancy velocity $U_b = \sqrt{g\beta\Delta TH}$, and temperature difference of $\Delta T = T_H - T_C$ (non-dimensional temperature is defined as $\theta = (T - \frac{1}{2}(T_H + T_C))/\Delta T$), the non-dimensional forms of the governing equations are given as,

$$\nabla \cdot \boldsymbol{u} = 0, \tag{2.1}$$

$$\frac{\partial \boldsymbol{u}}{\partial t} + \boldsymbol{u} \cdot \nabla \boldsymbol{u} = -\nabla p + \sqrt{\frac{Pr}{Ra}} \nabla^2 \boldsymbol{u} + \theta \boldsymbol{e_y}, \tag{2.2}$$

$$\frac{\partial \theta}{\partial t} + \boldsymbol{u} \cdot \nabla \theta = \frac{1}{\sqrt{PrRa}} \nabla^2 \theta, \tag{2.3}$$

where $\boldsymbol{u}$ is the velocity vector, p is the dynamic pressure and $\boldsymbol{e_y}$ unit vector along the y axis. We consider a constant Prandtl number of $Pr = \nu/\alpha = 1.0$, and the above system is then solely governed by the Rayleigh number (Ra) defined as

$$Ra = \frac{g\beta \Delta T H^3}{\nu \alpha}, \tag{2.4}$$

where ν is the kinematic diffusivity, α is the thermal diffusivity, g is gravity and β is the fluid's thermal expansion coefficient. We model the external flow as boundary-layer flow with arbitrary wall heating, albeit with different normalization quantities. The details behind the governing equations of the external flow are discussed in more detail in § 2.2.

2.1. *Numerical implementation*

The internal flow is modelled by discretizing equations (2.1)–(2.3) on a cell-centred, collocated (non-staggered) Cartesian grid. The variables u_i, p and θ are all defined at the cell centres. The face-centre velocities (U_i) are also computed. The discretized equations are integrated in time using a fractional-step method where an intermediate velocity u^* is first obtained iteratively using a line-successive over relation scheme. This is followed by a pressure correction step, and finally, the pressure and intermediate velocities are updated. A Crank–Nicolson scheme is used for the diffusion and advection terms. The resulting discretized momentum equation (using Einstein notation) is

$$\frac{u_i^* - u_i^n}{\Delta t} = \frac{1}{2}(H_i^{n+1} + H_i^n) + \frac{1}{2}(D_i^{n+1} + D_i^n) + \theta^n \tilde{\delta}_{i2}, \tag{2.5}$$

$$H_i = -\frac{\delta(U_j u_i)}{\delta x_j}, \quad D_i = \frac{Pr}{\sqrt{Ra}} \frac{\delta^2 u_i}{\delta x_j \delta x_j}, \tag{2.6a,b}$$

where H_i is the ith component of the advection terms, and $\tilde{\delta}_{i2}$ is the Kronecker delta, and u_i interpolated to the cell wall by averaging the adjacent cells; D_i represents the ith component of the diffusion term, and $\delta/\delta x_j$ represents a second-order central-difference scheme with respect to the coordinate x_j. Similar to a staggered grid approach, only the cell-face velocities are used to calculated the volume flux from each cell. The following averaging procedure is used:

$$\tilde{u}_i = u_i^* + \Delta t \frac{\delta p^n}{\delta x_i}, \tag{2.7}$$

$$\left.\begin{aligned} \tilde{U}_1 &= \gamma_W \tilde{u}_{1P} + (1 - \gamma_W)\tilde{u}_{1W}, \\ \tilde{U}_2 &= \gamma_S \tilde{u}_{2P} + (1 - \gamma_S)\tilde{u}_{2S}, \end{aligned}\right\} \tag{2.8}$$

$$U_i^* = \tilde{U}_i + \Delta t \frac{\delta p^n}{\delta x_i}, \tag{2.9}$$

where the subscripts P, W, S denote the centre cell as well as the west and south cells, respectively. Also, γ_W, γ_S are linear interpolation weights (for uniform grids $\gamma_i = 1/2$) for the corresponding cells, and Δt is the time step which is made certain to satisfy the Courant–Friedrichs–Lewy (CFL) condition at each iteration. This averaging procedure eliminates the odd–even decoupling that usually occurs with non-staggered methods and

suppresses spurious modes in the pressure field (Zang, Street & Koseff 1994; Ye *et al.* 1999). This interpolation technique for collocated grids was first pioneered by Rhie & Chow (1983) and has since been extended and modified to overcome certain setbacks in the original formulation. Here, the interpolation of the cell-centred velocity to the cell face disregards the fourth-order derivative term of the pressure field.

The second step in the fractional-step method requires solving the pressure correction equation

$$\frac{u_i^{n+1} - u_i^*}{\Delta t} = -\frac{\delta p'}{\delta x_i}. \tag{2.10}$$

The continuity equation is used here to make sure the final velocity u_i^{n+1} is divergence free. This gives rise to the following Poisson equation:

$$\frac{\delta}{\delta x_i}\frac{\delta p'}{\delta x_i} = \frac{1}{\Delta t}\frac{\delta U_i^*}{\delta x_i}. \tag{2.11}$$

This, along with a Neumann boundary condition imposed at all boundaries, is solved implicitly using a bi-conjugate gradient method with stabilization. The solution of this correction step is then used to update the pressure and velocity as

$$\left.\begin{aligned} p^{n+1} &= p^n + p', \\ u_i^{n+1} &= u_i^* - \Delta t\,\frac{\delta p'}{\delta x_i}, \\ U_i^{n+1} &= U_i^* - \Delta t\,\frac{\delta p'}{\delta x_i}. \end{aligned}\right\} \tag{2.12}$$

The energy equation is discretized similarly, resulting in

$$\frac{\theta^{n+1} - \theta^n}{\Delta t} = \frac{1}{2}(\tilde{H}^{n+1} + \tilde{H}^n) + \frac{1}{2}(\tilde{D}^{n+1} + \tilde{D}^n), \tag{2.13}$$

$$\tilde{H} = -\frac{\delta(U_j\theta)}{\delta x_j}, \quad \tilde{D} = \frac{1}{\sqrt{PrRa}}\frac{\delta}{\delta x_j}\frac{\delta\theta}{\delta x_j}. \tag{2.14a,b}$$

This discretization technique was first introduced by Zang *et al.* (1994) and has subsequently been shown to be an accurate method for incompressible flows. The methodology employed here has been validated extensively, reproducing both analytical solution of the Navier–Stokes equations and experimentally measured flow fields (Zang *et al.* 1994; Ye *et al.* 1999; Marella *et al.* 2005; Kim *et al.* 2008; Shoele & Mittal 2014; Ojo & Shoele 2021; Rips, Shoele & Mittal 2020). The method has also been used for simulation of turbulent flows (Salvetti *et al.* 1997; Yuan, Street & Ferziger 1999; Armenio & Sarkar 2002). The resulting discretized energy equation is solved using an alternating-direction implicit method imposing homogeneous Neumann boundary conditions at the top and bottom walls. The vertical wall boundary conditions are set as a CBC, quantifying the heat transfer from the external flows. This type of boundary condition is explained in the next section.

2.2. *Conjugate boundary conditions*

The external flow is represented with an analytical kernel. A kernel, $\mathcal{G}$, is constructed to model the temperature distribution in the external flow and therefore reduces the external

flow problem into a Fredholm equation of the first kind for the flux on the boundary

$$\tilde{\theta}\,(\boldsymbol{s}, t) = \int_S \int_0^t \mathcal{G}\,(\boldsymbol{s} - \boldsymbol{\xi}, t - \tau)\ \tilde{q}\,(\boldsymbol{\xi}, \tau)\,\mathrm{d}\tau\,\mathrm{d}\boldsymbol{\xi}, \tag{2.15}$$

where S is the surface described by the intrinsic coordinates $\boldsymbol{s} = (s_1, s_2)$, $\tilde{q}$ is the heat flux distribution on the surface S in the general three-dimensional configuration, where $\tilde{\boldsymbol{q}} = \tilde{q}\boldsymbol{n}$, and $\tilde{\theta}$ is the interface temperature between the internal and external flows.

To form the kernel, we consider the external flow as flow over a flat plate with free-stream flow velocity V, and a point source heat flux $q \cdot \delta(\boldsymbol{s} - \boldsymbol{\xi})$, where δ is the delta function. The heat from the point source is advected downstream, and diffuses in all directions. Although the focus of this study is on a two-dimensional enclosure, and therefore the external solution can be reduced to a single dimension along the vertical wall, the following formulation is presented in its general form for a two-dimensional plate and a three-dimensional enclosure. With a change in reference frame the point source is considered as a moving source and the fluid to be a quiescent medium. Thus, the system can be solved as pure conduction with a moving heat source, similar to the technique employed by Ortega & Ramanathan (2003). The heat kernel $\mathcal{K}_{diff}$ is the fundamental solution to the heat diffusion equation and can be written as

$$\mathcal{K}_{diff} = \frac{1}{8\rho c\sqrt{\pi\alpha t}} \exp\left[-\frac{(s_1 - \xi_1)^2 + (s_2 - \xi_2)^2}{4\alpha t}\right], \tag{2.16}$$

where (ξ_1, ξ_2) is the in-plane coordinate of the point source, α and c are the thermal diffusivity and specific heat of the fluid, respectively. We consider a moving source with heat flux rate of q moving a distance $V(t - t')$ between time t and t' with V being the free-stream velocity to modify (2.16) and calculate the temporal changes of temperature distribution on the plate

$$T(\boldsymbol{s}, t) = \int_S \int_0^t \frac{q(\boldsymbol{\xi})\,\mathrm{d}t'}{8\rho c[\pi\alpha(t - t')]^{1/2}} \exp\left[-\frac{\big(s_1 - \xi_1 - V(t - t')\big)^2 + (s_2 - \xi_2)^2}{4\alpha(t - t')}\right] \mathrm{d}\boldsymbol{\xi}. \tag{2.17}$$

The convective time scale of the external flow is assumed to be much faster than the time scale of the internal flow due to natural convection and therefore, only the steady-state part of (2.17) is kept. Furthermore, the formulation is rewritten for rectangular patches of size $\Delta s_1 \times \Delta s_2$ to facilitate coupling with the Cartesian grid of § 2.2 and to form the non-dimensional relation between the boundary temperature ($\tilde{\theta}$) and non-dimensional heat flux Q as

$$\begin{aligned}\tilde{\theta}(\boldsymbol{s}) = \int_S \frac{Q(\boldsymbol{\xi})}{2\sqrt{2}\,RePr} \int_0^\infty \left(\mathrm{erf}\frac{Y + A}{\sqrt{2u}} - \mathrm{erf}\frac{Y - A}{\sqrt{2u}}\right) \\ \times \left(\mathrm{erf}\frac{X + B - u}{\sqrt{2u}} - \mathrm{erf}\frac{X - B - u}{\sqrt{2u}}\right) \frac{\mathrm{d}u}{\sqrt{u}}\,\mathrm{d}\boldsymbol{\xi},\end{aligned} \tag{2.18}$$

where $X = Us_1/(2RePr)$, $Y = Us_2/(2RePr)$, $B = U\Delta s_1/(2RePr)$ and $A = U\Delta s_2/(2RePr)$. Equation (2.18) is employed to construct the analytical kernel for the calculation of the surface temperature for any arbitrary surface heat flux distribution. The method can be further extended to account for time-dependent flow conditions. Figure 2 shows the comparison of the thermal boundary layer solution using the present

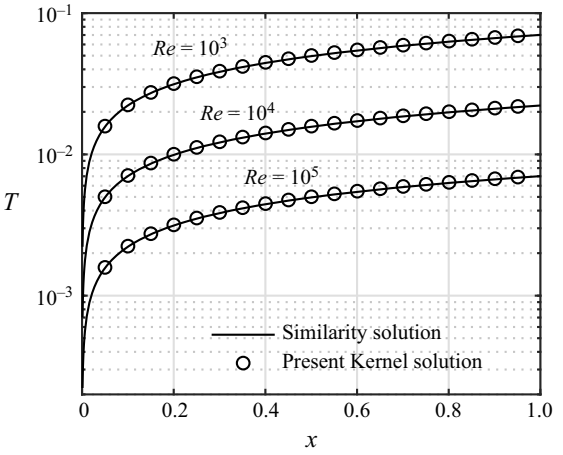

Figure 2. Surface temperature solution for a flat plate with constant heat flux. Comparison between the proposed kernel solution and the similarity solution by Bejan (2013).

method and the well-known von-Kármán–Polhausen integral method (Bejan 2013). The von-Kármán–Polhausen integral method solution uses assumed velocity and temperature profiles to integrate the momentum and energy equation across the boundary layer. As shown in figure 2, the temperature along the wall for a uniform heat flux is demonstrated for three different Reynolds numbers. The solutions are almost identical to the integral method for all cases tested.

2.3. *Boundary-layer approximation*

Gill (1966) proposed a theory known as the boundary-layer regime for differentially heated vertical enclosures. The theory provides an analytical solution to the DHC problem under certain conditions. The most important condition to form the analytical solution is the existence of two distinct flow regimes: (i) boundary-layer flow near the vertical sidewalls; and (ii) a recirculating core.

For a distinct core region to exist, the length of the enclosure (L) must be large compared with the boundary layers (δ), i.e. $L \gg \delta$. By scaling analysis, the following expression for δ can be derived:

$$\delta \sim H\left(\frac{Pr}{Ra}\right)^{1/4}, \tag{2.19}$$

which can be used to form the condition for the existence of a distinct core region as

$$\frac{L}{\delta} = AR^{-1}\left(\frac{Ra}{Pr}\right)^{1/4} \gg 1. \tag{2.20}$$

In the boundary-layer region, the steady-state dimensionless governing equations for high Ra flows are given as

$$\frac{1}{Pr}\left(u\frac{\partial v}{\partial x} + v\frac{\partial v}{\partial y}\right) = \frac{\partial^2 v}{\partial x^2} + \theta, \tag{2.21}$$

$$u\frac{\partial \theta}{\partial x} + v\frac{\partial \theta}{\partial y} = \frac{\partial^2 \theta}{\partial x^2}, \tag{2.22}$$

and subjected to the boundary conditions

$$u = v = 0, \quad \theta = \theta_w \quad at\ x = 0, \tag{2.23}$$

$$u \to u_0(y), \quad v \to 0, \quad \theta \to \theta_0(y) \quad as\ x \to \infty, \tag{2.24}$$

where u_0 and θ_0 are unknown flow and temperature in the core. Following Gill (1966), the Oseen-linearization technique is employed here to replace the u and $\partial\theta/\partial y$ factors in (2.21) and (2.22) with their average values of u_A and θ'_A, thereby removing all nonlinearities. Although the presented analysis is formulated for large Pr flows, it has been noted that it still valid for $Pr = O(1)$ (Gill 1966; Bejan 1979, 2013). The combination of the resulting linear equations forms a fourth-order ordinary differential equation of,

$$\frac{\partial^4 v}{\partial x^4} + u_A \frac{\partial \theta}{\partial x} + \theta'_A = 0. \tag{2.25}$$

The solution of which, in its general form, is

$$v = \sum_{n=1}^{4} a_n(y) \exp[-\lambda_n(y)\, x]. \tag{2.26}$$

Here, $\lambda_n(y)$ are the four roots of $\lambda^3(\lambda + u_A) + \theta'_A = 0$. The solution is valid for the entire boundary layer and when the boundary conditions (2.23) and (2.24) are applied, a general solution for velocity and temperature can be obtained as

$$v = \frac{\theta_w - \theta_0}{\lambda_2^2 - \lambda_1^2}(-\mathrm{e}^{-\lambda_2 x} + \mathrm{e}^{-\lambda_1 x}), \tag{2.27}$$

$$\theta = \frac{\theta_w - \theta_0}{\lambda_2^2 - \lambda_1^2}(\lambda_2^2 \mathrm{e}^{-\lambda_2 x} - \lambda_1^2 \mathrm{e}^{-\lambda_1 x}). \tag{2.28}$$

The boundary-layer equations governing the left and right sides of the enclosure are formed similarly. The centrosymmetric property of the problem is exploited to write the odd and even parts of the equations providing the necessary set of governing equations for the left and right sides of the enclosure. The Kármán–Polhausen integral method is used to relate the values of u_A, θ'_A, u_0 and θ'_0 through the even and odd parts of the mass and heat conservation integrals (Appendix A). Finally, to close the model, the boundary condition (2.23) at the wall is used to relate $\partial\theta/\partial n$ and θ_w as

$$\theta_w(y) = \int_0^H \mathcal{G}(y - \zeta) \left.\frac{\partial \theta(y, x)}{\partial x}\right|_{wall} \mathrm{d}\zeta, \tag{2.29}$$

where the kernel $\mathcal{G}$ is equal to the delta function if the boundary condition is isothermal, otherwise it is defined in § 2.2 in the case of CBCs. The model can be used to derive the Nusselt number (Nu) defined as

$$Nu = \frac{L}{H} \int_0^{AR} \left.\frac{\mathrm{d}\theta}{\mathrm{d}x}\right|_{x=0} \mathrm{d}y. \tag{2.30}$$

It can be shown that (2.30), with the profiles defined in (2.27) and (2.28), leads to the following Nu in the large Ra limit

$$Nu = 0.364 \frac{L}{H} Ra^{1/4}. \tag{2.31}$$

The power-law scaling of $Nu \sim Ra^{1/4}$ has been debated, but it is generally accepted that the exponent is in the range $1/3 - 1/4$ (Ng *et al.* 2015).

3. Results and discussion

Here, the direct numerical simulations of the differentially heated cavities coupled with the external flow CBCs are presented. Specifically, the parameters explored are aspect ratios $AR = 2, 4, 6, 8$, the internal Rayleigh numbers $Ra = 10^7, 10^8, 2 \times 10^8$ and the external Reynolds numbers $Re = 10^3, 5 \times 10^3, 10^4$. All simulations are performed on a uniform grid.

Through the grid convergence study, it is found that $\mathrm{d}x = \mathrm{d}y = 0.004$ is sufficient to accurately calculate the wall Nusselt number. Previous studies have shown that the important unsteady flow structures are not always confined to the near-wall region but can also be propagated through the entire domain (Xin & Le Quéré 2006). Therefore, the mesh is kept uniformly refined throughout the entire domain to accurately capture all relevant flow structures and instabilities, as well as to avoid any grid-dependent artificial diffusion from that may dissipate these modes. The convergence study is performed to determine the time step, Δt. The time step is dependent on Ra and defined such that it satisfies the CFL condition at each time iteration. We note that a time step of $O(10^{-4})$ is smaller than needed for stability reasons but was chosen to capture the coupling with the CBC accurately. The steady-state condition is associated with the situation in which the short-window (50 s) time-averaged Nusselt number changes less than 0.1 %.

3.1. *DHC with isothermal boundary conditions*

The response of a system with isothermal boundary conditions is discussed first. We then compare the system's thermal performance with the isothermal boundary condition and different CBC configurations.

3.1.1. *Temperature and flow fields*

The time-average streamlines and isotherms for all aspect ratios and Ra are shown in figure 3 for statistically steady-state/converged systems. The flow field of all cases consists of boundary-layer flow, identified by the vertical layers of thermally stratified flow near the vertical sidewalls and a distinct circulating core region. The smaller aspect ratio cases, such as $AR = 2, 4$, exhibit a separation region at the top and bottom horizontal walls, becoming more pronounced as Ra increases. This is driven by the thermal plume generated in the near-wall region due to higher local Ra. The impingement creates the backflow and results in separation at the top and bottom of the enclosures. The small AR cases also exhibit nearly horizontal isotherms in the core region. On the other hand, the large AR cases have very different flow and temperature fields with no flow separation at the top or bottom of the enclosure. While still exhibiting a vertical stratification, the isotherms are no longer horizontal in the core region. In all cases, except for $AR = 8$ and $Ra = 10^7$, a clear coherent core flow is formed. For $AR = 8$ and $Ra = 10^7$, the boundary layers from both sides of the enclosure grow close enough together to obscure a distinct core region.

From the constraint given by (2.20), the ratio L/δ, for the enclosure with $AR = 8$ and $Ra = 10^7$, is of $O(1)$, explaining the nearly indiscernible core region. For all aspect ratios and $Ra = 2 \times 10^8$, the streamlines lack symmetry from the top to bottom halves because the flow is non-stationary and exhibits time-dependent behaviour. However, for large AR, it is not obvious that the flow is no longer stationary for $Ra = 2 \times 10^8$. This will be more evident in the following sections.

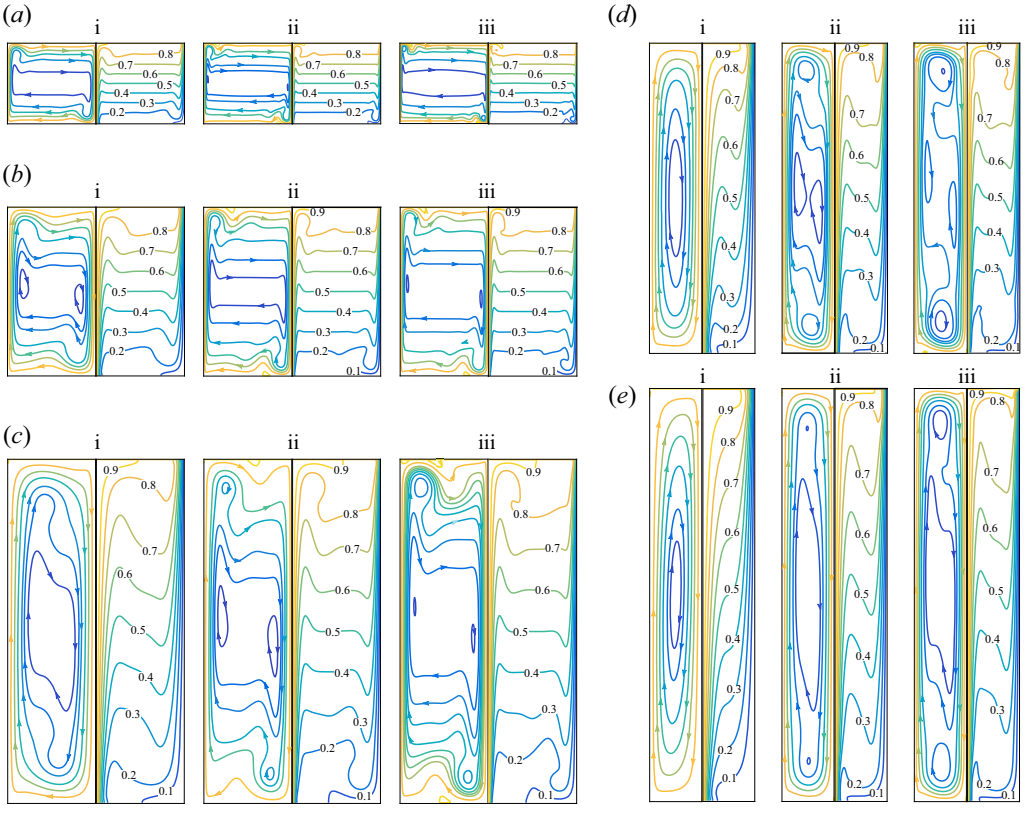

Figure 3. Streamlines (left of pair) and temperature contours (right of pair) for enclosures with isothermal boundary conditions. Each row corresponds to a specific aspect ratio (*a*) $AR = 1$, (*b*) $AR = 2$, (*c*) $AR = 4$, (*d*) $AR = 6$, (*e*) $AR = 8$. (i $- Ra = 10^7$, ii $- Ra = 10^8$, iii $- Ra = 2 \times 10^8$).

3.1.2. *Thermal performance*

The thermal performance is characterized by the average Nusselt number defined in (2.30). Different correlations have been proposed for Nu of tall enclosures following Gill's work (Ganguli *et al.* 2009). Among them, Bejan (1979) proposed the following correlation for tall enclosures:

$$Nu = C_B \left[\frac{Ra}{Pr\,AR}\right]^{0.25} \int_{-g_e}^{g_e} \frac{(1-g)^6(1+g)^2(7-g^2)}{(1+g^2)(1+3g^2)^{14/3}}\,\mathrm{d}g, \tag{3.1}$$

where C_B and g_e are functions of $(H/L)Ra_L^{1/7}$ (Bejan 1979). Here, $Ra_L = (L/H)^3/Ra = g\beta\Delta TL^3/\nu\alpha$ is the Rayleigh number defined based on the width L, instead of the height H as the characteristic length scale. While it is generally agreed that $Nu \sim Ra^{1/4}$, multiple studies have proposed slight modifications to this relation based on their observations. For example, another widely used correlation proposed by El Sherbiny *et al.* (1982) is

$$Nu = \max\left(Nu_1, Nu_2, Nu_3\right), \tag{3.2}$$

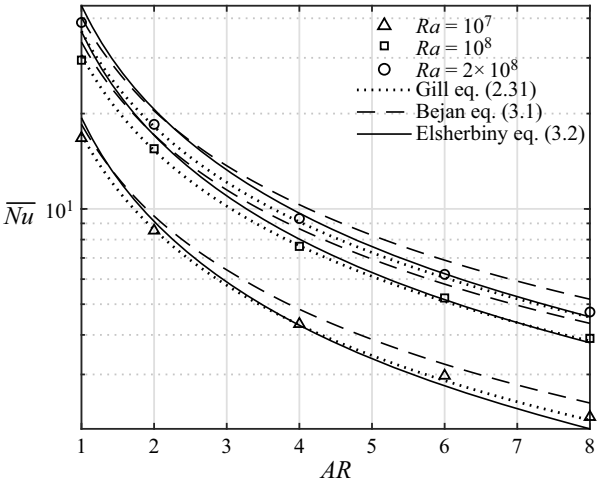

Figure 4. Comparison of the average Nusselt number calculated by the direct numerical simulations (symbols) with the correlations given in the literature (Gill 1966; Bejan 1979; El Sherbiny, Raithby & Hollands 1982).

where Nu_1, Nu_2, and Nu_3 are calculated from

$$\left.\begin{aligned} Nu_1 = 0.0605 Ra_L^{1/3}, \quad Nu_2 = \left[1 + \left[\frac{0.104 Ra_L^{0.293}}{1 + \left(\frac{6310}{Ra_L}\right)^{1.36}}\right]^3\right]^{1/3}, \\ Nu_3 = 0.242\left(\frac{Ra_L}{AR}\right)^{0.272}. \end{aligned}\right\} \tag{3.3}$$

Figure 4 shows a comparison of Nu calculated by (2.31) (dotted lines), Bejan's equation (3.1) (dashed lines) and Elsherbiny's equation (3.2) (solid lines) along with the values from the present study (symbols). Bejan's correlation has been shown to over-predict the Nusselt number (Turan *et al.* 2012). Elsherbiny's correlation was proposed for $AR > 5$, and it produces satisfactory results in that range. However, it also over-predicts the Nu for smaller aspect ratio enclosures. Correlation (2.31) is based on the boundary-layer model discussed in § 2.3. The temperature solution (2.28) is based on an exponentially decreasing profile approaching the core temperature T_0, and therefore, the Nusselt number directly depends on the temperature difference of the wall and core, $\Delta T = T_H - T_0$, instead of the temperature difference of the enclosure walls, $\Delta T = T_H - T_C$, as it is usually defined for DHCs. The variation of T_0 with respect to y is disposed of by taking the centreline ($y = H/2$) or mean value $T_0 = \frac{1}{2}(T_H + T_C)$. Therefore, we define Ra based on $\Delta T = T_H - \frac{1}{2}(T_H + T_C)$ noting that this temperature difference also appears in the Gill's so-called centrosymmetric property of differentially heated enclosures (Gill 1966). In doing so, (2.31) gives a much better Nu prediction (see figure 4 dotted curve), the present results (symbols) are in nearly perfect agreement with this correlation. At the end, this translates into a factor of $1/2$ in the Ra and a factor of $(0.5)^{0.25} = 0.8409$ in the calculation of Nu.

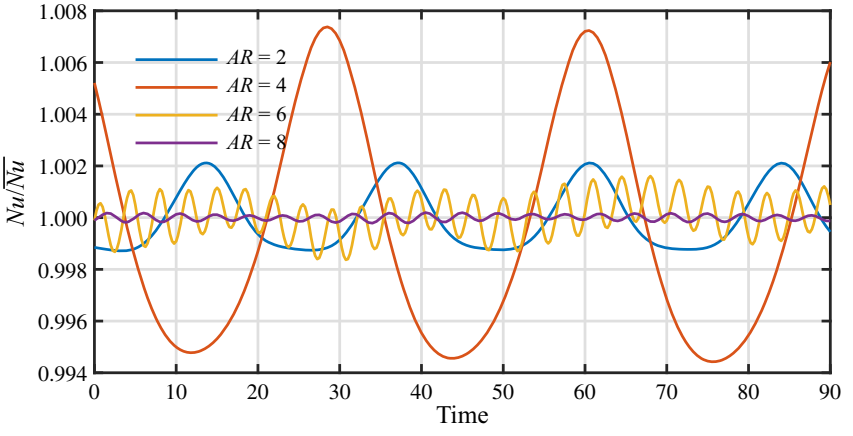

Figure 5. Wall-average Nusselt number time dependence for $Ra = 2 \times 10^8$.

3.1.3. *Time dependency and instability modes*

As discussed in § 3.1.1, periodic time-dependent flow is observed for several cases. Time-dependent flow has been reported to exist only if Ra exceeds a critical value (Ra_c), which depends on AR (Paolucci & Chenoweth 1989; Christon *et al.* 2002; Xin & Le Quéré 2006). Specifically for $AR = 2, 4, 6, 8$, the critical Rayleigh number at which time-dependent flow emerges is $Ra_c = 1.59 \times 10^8$, 1.03×10^8, 1.11×10^8 and 1.57×10^8 respectively, as reported by Xin & Le Quéré (2006). Here, only $Ra = 2 \times 10^8$ cases are above the critical value for all AR values, and this is why only these cases exhibit time-dependent behaviour. This is further illustrated in figure 5 by plotting the time variations of $Nu/\overline{Nu}$ for $Ra = 2 \times 10^8$ cases, where $\overline{Nu}$ denotes the time-averaged quantity of Nu. While consistent oscillatory behaviour is observed for these set-ups, the magnitude and frequency are different. The low AR enclosures exhibit low-frequency oscillation compared with the high AR enclosures due to the instability mechanism. We will discuss this effect later, along with the different instability modes. The magnitude of the oscillations shown in figure 5 increase as Ra increases beyond Ra_c. When $AR = 4$, the oscillation amplitude of $Ra = 2 \times 10^8$ is approximately twice Ra_c, while there is only 25 % increase compared with Ra_c for $AR = 2$. The higher amplitude fluctuations is observed for $AR = 4$ enclosure.

The characteristic mode associated with the transition to time-dependent flow is of special interest and has also been reported by Xin & Le Quéré (2006) wherein the modes are obtained from the linear stability analysis. From our direct numerical simulation results, extraction of the relevant modes is possible via modal decomposition techniques (Taira *et al.* 2017; Ramos *et al.* 2019; Vijayshankar *et al.* 2020). The well-known dynamic mode decomposition (DMD) pioneered by Schmid (2010) is used here to gain insight into the characteristic modes of the flow.

The flow data are represented by the matrix $\boldsymbol{M} = [\boldsymbol{m}(t_1)\ \boldsymbol{m}(t_2)\ \cdots \boldsymbol{m}(t_n)]$, where $\boldsymbol{m}(t_i)$ is the snapshot of the flow velocity and temperature at time t_i. DMD finds the best transition matrix $\boldsymbol{A}$ such that

$$\boldsymbol{M}_{2:n} = \boldsymbol{A}\boldsymbol{M}_{1:n-1}. \tag{3.4}$$

DMD modes and the associated frequencies are calculated using the singular value decomposition of the data matrix as follows Schmid (2010)

$$\boldsymbol{M}_{1:n-1} = \boldsymbol{U}\,\boldsymbol{\Sigma}\,\boldsymbol{V}^{T}. \tag{3.5}$$

Defining $\tilde{\boldsymbol{A}} = \boldsymbol{U}^{T}\,\boldsymbol{M}_{2:n}\,(\boldsymbol{V}\boldsymbol{\Sigma}^{-1})$, the eigenvalues μ_j and eigenvectors $\boldsymbol{\phi}_j$ of $\tilde{\boldsymbol{A}}$ can be found and used to calculate

$$\lambda_j = \frac{1}{\Delta t}\log(\mu_j), \quad f_j = \frac{\mathrm{ang}\,(\lambda_j)}{2\pi}, \tag{3.6a,b}$$

where $\mathrm{ang}(\lambda_j)$ is the phase angle of the complex eigenvalue λ_j, and $\Delta t = t_{i+1} - t_i$ is the time difference between data snapshots.

For buoyancy-driven flows, the coupled dynamics between the temperature and velocity field is critical, and therefore, the data vector is defined to preserve this coupling. Moreover, the decomposition in DMD must be accompanied by a choice of inner product and the corresponding norm or pseudo-energy function. The temperature and velocities are both used to form the observed data vector, $\boldsymbol{m} = \{\gamma\theta, u, v\}^{\mathrm{T}}$. The scaling factor $\gamma = \langle uu + vv\rangle/\langle\theta\theta\rangle$ is adopted to make the dissimilar quantities of temperature and velocity consistent and energies comparable (Lumley & Poje 1997; Hasan & Sanghi 2007; Puragliesi & Leriche 2012). The number of snapshots used to calculate modes depends on the period of oscillation of the *Nu* for each case. At least 10 complete periods of the *Nu* oscillation are included in the data matrix $\boldsymbol{M}$. The time between snapshots is $\Delta t = 0.5$ which corresponds to a sampling frequency of 2. This is much larger than the highest anticipated the *Nu* variation frequency of 0.1. The number of snapshots used to calculate the modes was varied from 80 to 300. As long as at least one complete period of the *Nu* oscillations was included, the results were similar within 1 % accuracy.

The dynamic modes associated with the time-dependent behaviour are shown in figure 6 for $AR = 1, 2, 4, 6, 8$. Two distinct modes can be identified: those observed only in the small AR cases and the mode observed only in the large AR cases. A similar observation has been made previously by Xin & Le Quéré (2006) in which they found two types of modes: the first mode was observed in enclosures with the small aspect ratios $AR < 3$ (henceforth referred to as $\boldsymbol{\phi}_s$) and the other was observed for the large $AR \geq 4$ (henceforth referred to as $\boldsymbol{\phi}_l$). They associated the first mode, $\boldsymbol{\phi}_s$ with angled internal waves encompassing the entire enclosure (similar to what is shown for $AR = 1$ in figure 6). This mode is generated by the separation at the end of the vertical boundary layers where the flow impinges the top and bottom horizontal walls. However, there has not been a consensus about what physical mechanism causes instability. They described the second mode as a travelling wave mode confined to the boundary layer (similar to $AR = 8$ in figure 6).

In this study, we also observed the two modes reported by the stability analysis of Xin & Le Quéré (2006). However, it is $\boldsymbol{\phi}_s$ and not $\boldsymbol{\phi}_l$ that is present in $AR = 4$, different from the Xin and Le Quere's prediction. We note that the modes reported by them were for systems at the critical Rayleigh number, Ra_c, and our system is in the supercritical range ($Ra = 2 \times 10^8 > Ra_c = 1.03 \times 10^8$). The streamlines for this case (figure 3) clearly show a separation region that is associated with $\boldsymbol{\phi}_s$. The frequency of this mode is $f = 0.032$, the same as the frequency of the *Nu* time history shown in figure 4. We are confident that $\boldsymbol{\phi}_s$ is the time-dependent mode for our system. The large AR cases clearly show a travelling wave disturbance consisting of alternating positive and negative temperature fluctuation regions near the cavity walls. This mode travels in the clockwise direction and is similar to the unstable modes reported in the literature for the current configuration (Christon *et al.* 2002; Xin & Le Quéré 2006). Like the small aspect ratio cases, the frequency associated

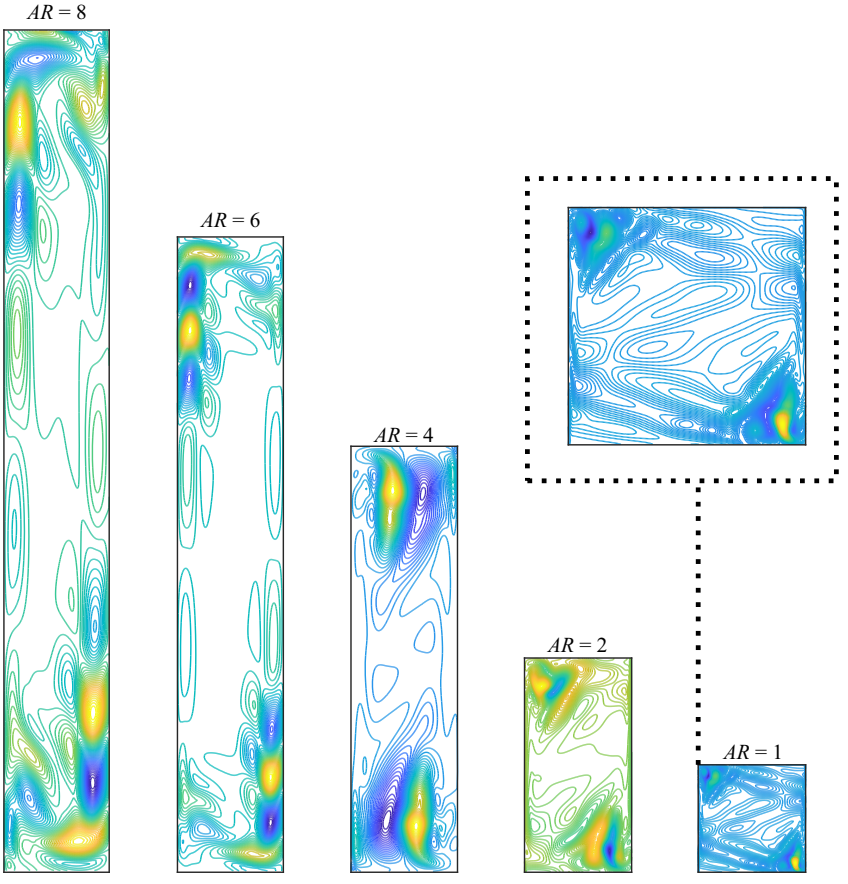

Figure 6. Time-dependent DMD modes for all aspect ratios and $Ra = 2 \times 10^8$. Only $Ra = 2 \times 10^8$ exhibits time-dependent modes.

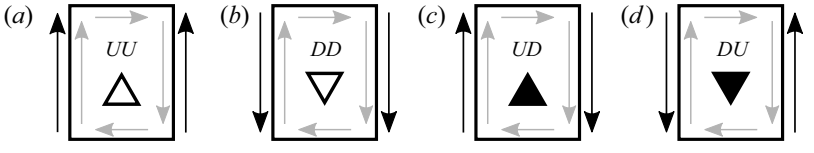

Figure 7. Configurations of the CBC and associated labels based on the direction of the external flow.

with these modes matches the fluctuation frequency of Nu, with $f = 0.43$ and 0.21 for $AR = 6$ and 8 respectively.

3.2. *DHC with CBCs*

The configuration of the CBC can take four different conditions as shown and labelled in figure 7. The arrows on either side of the square represent the external flow direction, while the gravity always acts along the $-y$ axis. Each configuration will be referred to by the first letter of external flow directions, e.g. UD corresponds to Up on the left and Down on the right (third configuration in figure 7). The effects of AR, and Ra are studied for the same values as the previous section.

3.2.1. *Effects on Nusselt number*

The heat transfer of the system depends on the internal flow, characterized by Ra, and the external flow, characterized by Re. The heat transfer at the wall can be treated as a lumped element system to explain the effects of the internal and external flows on the heat transfer and is written as $Q = \Delta T_w/R$. Here, ΔT_w is the temperature difference across the wall, and R is the thermal resistance between the external and internal flow. Assuming zero thermal resistance from the wall (thin membrane), the total thermal resistance R is a series of resistances due to the external boundary layer, $R_{ex} \sim k^{-1}Re^{-0.5}$, and internal boundary layer, $R_{in} \sim k^{-1}Ra^{-0.25}$ (Shu & Pop 1999). This suggests that the ratio of thermal resistances $\Omega = R_{in}/R_{ex} = Re^{0.5}Ra^{-0.25}$ can be employed to describe how the normalized Nusselt number changes as plotted in figure 8. The ratio Ω can also be viewed as the ratio of the boundary-layer thickness of the external flow to the boundary-layer thickness of the internal flow. Therefore, a higher ratio represents a thinner external boundary layer relative to the internal flow. The symbols in figure 8 are based on what has been defined in figure 7. In figure 8 the isothermal boundary condition limit (dotted line) of the normalized Nusselt number is approached as the ratio Ω increases for all configurations of CBC. We can see that, for lower Ω, the difference in Nu between the different configurations is more significant. As Ω increases, this difference between the configurations decreases as all configurations approach the isothermal limit. Specifically, for the case of $AR = 4$, the isothermal boundary limit (- -) is not monotonically approached like the other cases.

With respect to the influence of the configuration of the external flow, a clear trend is observed. The DU (▼) configuration has the highest heat transfer among all CBC cases, while the UD (▲) configuration has the lowest. The other configurations, UU and DD, show almost identical thermal characteristics in all cases. The heat transfer across the left enclosure wall is comprised of either parallel flow when the CBC is UD or UU, or counterflow when the CBC is DU or DD. This is true as long as the internal flow circulates in a clockwise fashion. A similar observation can be made for the right wall, parallel flow with the UD and DD CBC, and counterflow with DU and UU CBC. From the study of heat exchangers, it is known that the counterflow configurations always yield higher heat transfer rates. By comparison, it is not surprising that the DU CBC would yield the best heat transfer amongst the CBC cases since it has a counterflow configuration at both sidewalls.

The lower Nusselt number resulting from the boundary condition cases compared with the isothermal case is explained by the reduction of the average wall temperature due to the CBCs. The reduction in the average wall temperature effectively reduces the Rayleigh number of the system. The isothermal case can be viewed as a conjugate boundary case with infinite (or very large) Reynolds number flow, such that the temperature of the walls is unaffected. This may be very hard to achieve in practical applications or very costly. Therefore figure 8 is a comparison of the Nusselt number for various external flow speeds and the ideal infinite velocity (i.e. isothermal) case.

In addition to the computational results in figure 8, the analytical model of § 2.3 is applied to an enclosure with CBCs. The effects of the conjugate boundary condition on the Nusselt number are effectively captured in the multiplicative constant in (2.31). Due to the centrosymmetric restriction of the analytical model, only the UD and DU configurations are considered here, and the results are shown in figure 8 (blue symbols). Like in the isothermal boundary condition case, the boundary-layer model successfully predicts the thermal performance of most cases. However, we again see that the $AR = 4$ cases in the vicinity of $Re^{0.5}/Ra^{0.25} \approx 1$, deviate from the boundary-layer model.

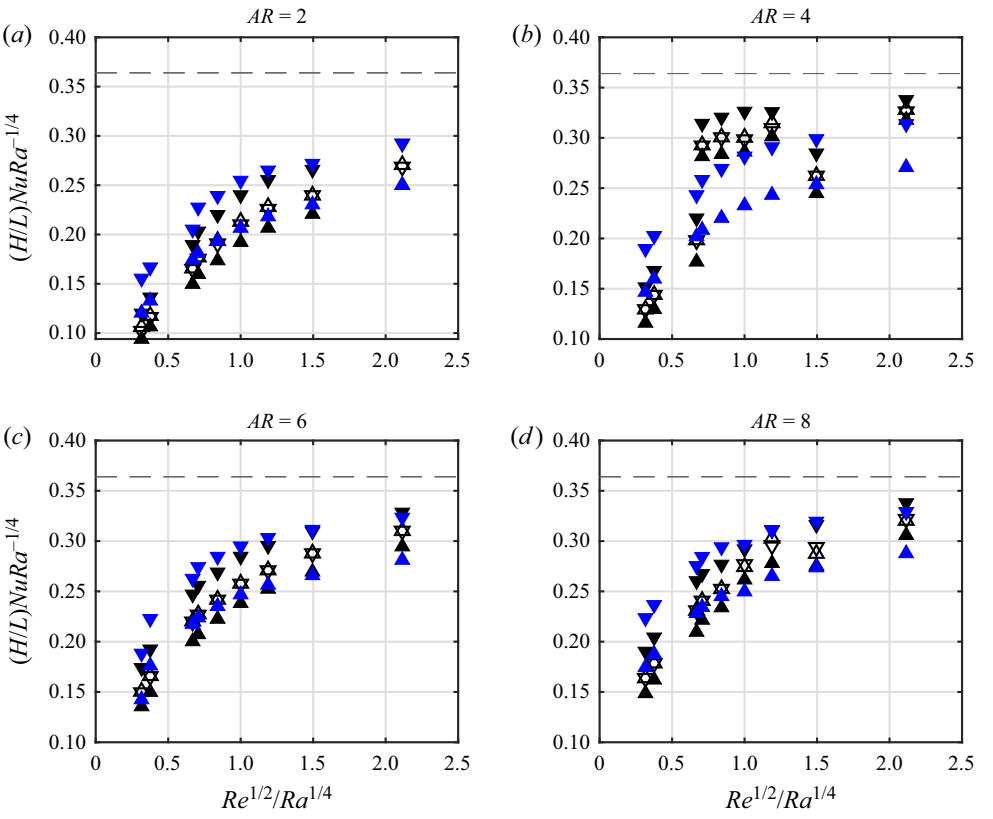

Figure 8. Comparison of the normalized Nusselt number with respect to the ratio of the internal and external boundary-layers thickness ($\Omega = Re^{0.5}/Ra^{0.25}$) between the direct numerical simulation (DNS) results and boundary-layer model. See figure 7 (UD configuration ▲) (DU configuration ▼) (DD configuration ▽) (UU configuration △) (boundary-layer model UD configuration ▲, blue) (boundary-layer model DU configuration ▼, blue) ((2.31) - -).

Closer inspection of these cases (figure 9) shows the higher than expected Nu is due to a relatively higher mean free-stream velocity $\bar{v}$ and thinner boundary-layer thickness δ. Unlike natural convection from a heated vertical plate, where the mean streamwise velocity ($\bar{v}$) is zero, $\bar{v}$ is non-zero for differentially heated vertical enclosures. Here, we define $\bar{v}$ as the maximum near-wall velocity along the height of the enclosure. The associated internal boundary-layer thickness can then be defined as $\delta = -(\Delta T/2)/(\mathrm{d}\theta/\mathrm{d}x|_w)$ (Zhou & Xia 2010; Zhou *et al.* 2010; Scheel & Schumacher 2014; Ng *et al.* 2015). We note that the boundary layers on the left and right walls are similar but develop in opposite directions, i.e. the left wall boundary layer develops in the $+y$ direction while the right wall boundary layer develops in the $-y$ direction. Additionally, the boundary layers are only similar if the flows are similar. This means that the right wall boundary layer with a CBC direction U (UU or UD configurations) is similar to a left wall boundary layer if the left wall CBC direction is D (DD or UD configurations).

A thin boundary layer results in higher heat transfer and therefore higher $\bar{v}$ which ultimately leads to the impingement of the buoyant jet on the top and bottom walls on the left and right side of the enclosure, respectively. The impingement creates a separation region and secondary vortex near the ends of the side edges, which is the direct cause of the thinner boundary layer on the opposite side. The impingement and separation phenomena

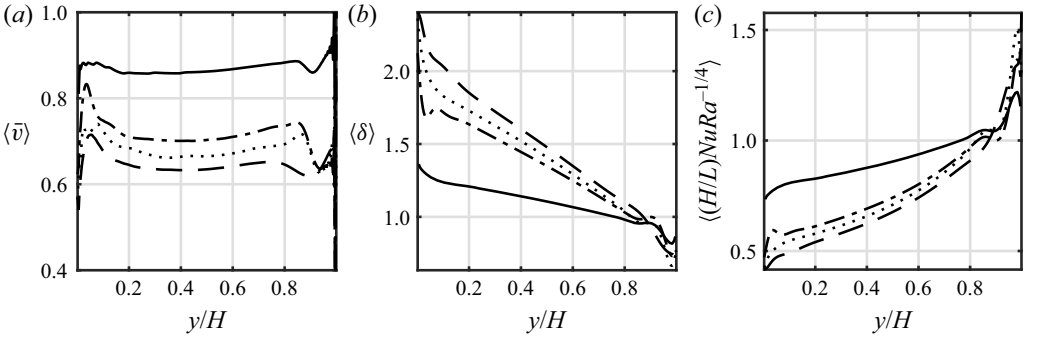

Figure 9. Cases; (- -) $AR = 4$, $\Omega = 0.67$; (-) $AR = 4$, $\Omega = 0.71$; (-.) $AR = 6$, $\Omega = 0.71$; (:) $AR = 2$, $\Omega = 0.71$. (*a*) Mean free-stream velocity, (*b*) boundary-layer thickness and (*c*) normalized Nusselt number. Here, $\langle\cdot\rangle$ denotes normalization of the argument by the corresponding isothermal case value.

only occur in smaller aspect ratio cases (see figure 3). Similarly, the $AR = 2$ enclosure exhibits the separation region at the end of the boundary layers as shown in figure 3(*b*). However, due to the wide aspect of the enclosure, the secondary vortex is relatively far from the opposite wall. Here, the separation and secondary vortex are positioned at $x/L \approx 0.25$ compared with $x/L \approx 0.6$ in the $AR = 4$ enclosure. This allows for the flow to reattach in the $AR = 2$ case, and the opposite wall boundary layer is not affected in the same way as in the $AR = 4$ enclosure. We note that only in the cases with $Re^{0.5}/Ra^{0.25} \approx 1$ for $AR = 4$, is the $\bar{v}$ high enough to create the separation region. In all other cases, the flow remains attached due to the reduction in the wall temperature, which leads to low $\bar{v}$.

While the increase in Nu is explained by the thinning of the boundary layer, the same cannot be said for the deviation of the boundary-layer model at these points ($Re^{0.5}/Ra^{0.25} \approx 1$). Unlike the isothermal case where the thermal capacity near the wall is reached before the end of the wall, CBC cases have a reduced wall temperature and therefore do not reach the full thermal capacity until the end of the wall. Indication of this is seen in 9(*c*) as the normalized Nu is larger than unity for $y/H \geq 0.75$, which shows that in the isothermal case, the Nu is defined primarily at the beginning of the wall and would not be significantly affected by secondary vortex and separation region at the end of the boundary layer. On the other hand, the CBC cases depend on the entire height of the wall to reach the thermal capacity, and the overall Nu is affected by the end wall effects. Due to the linearization of the boundary-layer model, the end wall separation effect cannot be modelled and results in the less than perfect prediction of the heat transfer in the $AR = 4$ and $Re^{0.5}/Ra^{0.25} \approx 1$ cases.

A power-law scaling of $Nu \sim a(H/L)^b\, Ra^c$ is employed to predict the overall heat transfer in the CBC configuration. A similar relation has been tried for the problem of conjugate boundary layers of free convection on either side of a vertical wall (Anderson & Bejan 1980; Treviño, Mendez & Higuera 1996). The difference is that, here, one side is forced convection and the other is natural convection, instead of both sides being natural convection. However, the principle is the same. In fact, when $Re^{0.5}Ra^{-0.25} = 1$ in the DU configuration, the external and internal boundary-layer thicknesses are similar and the system is equivalent to the case examined in Anderson & Bejan (1980). Using the boundary-layer model of CBC configurations, the coefficients ($Nu \sim a(H/L)^b Ra^c$) are identified as a function of Re as $a = -1.1Re^{-0.24} + 0.364$, $b = 1.3Re^{-0.19} - 1$, $c = -0.2Re^{-0.23} + 0.25$. The correlation approaches the isothermal boundary case (2.31) in the high Re limit. The predictions from the proposed relation are compared with the

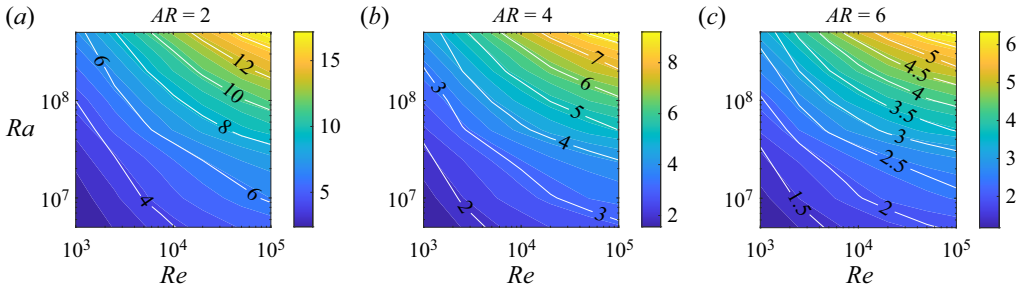

Figure 10. Comparison of the fitted *Nu* correlation (white contours) and the boundary-layer model (colour map).

boundary-layer model results (colour) in figure 10 for different *Re*, *Ra* and selected aspect ratios where in the power-law relation agrees well with the theoretical boundary-layer model.

3.2.2. *Equivalent heat flux and Rayleigh number*

In the previous section, we compared the thermal performance of the CBC cases at an equivalent external fluid temperature. Due to the CBC, the average wall temperature, and therefore the effective Rayleigh number was lower than the isothermal case. To reach a more pertinent comparison, in figure 11, the CBC cases and isothermal boundary condition DHC are compared at the same mean wall temperature, i.e. at the same effective Rayleigh number based on the temperature difference between two vertical walls (Ra_{eff}). In figure 11(*a*,*b*) the ratio of CBC and isothermal cases heat fluxes are compared for two different *Ra* for a typical external Reynolds number of $Re = 5 \times 10^3$. Note that the title denotes *Ra* based on the external fluid temperature of the CBC; however, each point has an associated Ra_{eff} at which an isothermal boundary condition case is compared. The heat flux of the CBC cases decreases with respect to the isothermal cases as *AR* increases. It can also be observed that the difference between the different CBC configurations decreases as *AR* increases. The difference between CBC configurations is also larger for the higher *Ra* case, as is the CBC case heat fluxes compared with the isothermal case heat fluxes. In figure 11(*c*,*d*), the ratio of heat fluxes of the CBC and isothermal cases are shown for different external flow *Re* and a fixed $Ra = 10^8$. Similar trends are observed here; the CBC case's heat flux and the difference between CBC configurations decrease with increasing *AR*. We can see that as Ω, the ratio of internal to external thermal resistance defined in § 3.2.1, increases the differences between the CBC cases decreases. Looking at only the UD and DU configurations, which bound the data curves, it is clear that the difference between different CBC configurations is associated with the reduction in heat flux of the DU configurations. The UD, or parallel-flow configuration, cases always have approximately the same heat flux as the equivalent Ra_{eff} isothermal case. It is interesting that for an equivalent Ra_{eff}, the heat flux q from CBC configurations is higher than that of the isothermal boundary condition cases for most cases.

While the average wall temperature difference is similar between the CBC and isothermal cases, the temperature profile along the walls is significantly different, as shown in figure 12. This leads to an increase in the heat flux compared with the isothermal case. Figure 12 shows the wall temperature profiles for select CBC cases normalized by the mean wall temperature, i.e. the isothermal boundary case with a uniform temperature profile. Two distinct shapes are observed corresponding to either a parallel or counterflow

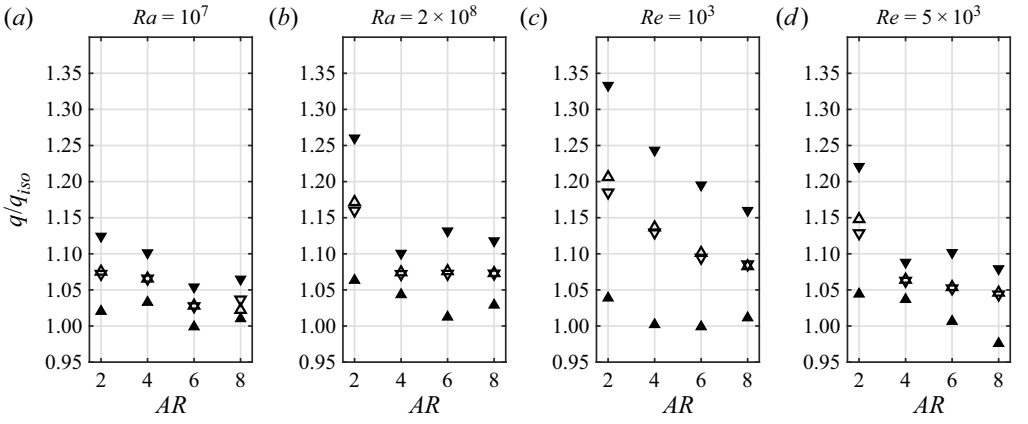

Figure 11. The ratio of the heat flux q of CBC cases to the heat flux q_{iso} of an equivalent isothermal boundary case at an equivalent Rayleigh number Ra_{eff} for different AR values; (a,b) are for two Ra cases with $Re = 5 \times 10^3$, and (c,d) are for two representative Re cases with $Ra = 10^8$.

configuration at each wall. For example, the UU and UD configurations at the left wall (figure 12a,c) exhibit a parallel-flow configuration at the left wall and thus have a concave temperature profile. A similar profile is found along the right wall for the DD and UD configurations. The other observed temperature profile corresponds to the counterflow configuration, i.e. DD and DU configurations at the left wall (figure 12b,d) and the UU and DU configurations at the right wall (figure 12a,d). This profile monotonically increases along the wall's height with respect to the isothermal profile. Both types of temperature profiles increase the stratification of the core temperature in the mid-height region leading to higher heat transfer overall.

3.2.3. *Effect on flow and time-dependent modes*

The effects of the conjugate boundaries extend beyond just the system's heat transfer. Differences in the streamlines and isotherms are hard to discern; instead, the dominant dynamic modes can be used to inspect the flow dynamics. The procedure discussed in § 3.1.3 is applied to the results obtained from the simulations of a cavity with CBCs. The external heat transfer in the CBC cases reduces the average wall temperature, thereby lowering the effective Ra (defined based on the wall temperatures). For the case with a large aspect ratio of $AR = 8$ and $Re < 10^4$, the reduction in the wall temperatures due to the external flow was sufficient to bring the system well below the critical Rayleigh number. Consequently, the system no longer exhibits the time-dependent characteristics observed in the isothermal case discussed in § 3.1.3. For $Re = 10^4$ cases, the effective Ra remains above the critical value and the dynamic mode associated with time dependence is observed for all configurations of the CBC.

For the $AR = 6$ enclosure, the effective Ra remains above Ra_c for all configurations if $Re \geq 10^4$. Surprisingly, only the UD configuration exhibits the time-dependent mode associated with this aspect ratio ($\boldsymbol{\phi}_l$). The UD configuration, also referred to as the parallel-flow configuration, seems to be the only configuration to excite the instabilities leading to the time-dependent behaviour. While the $AR = 6$ case does exhibit the time-dependent mode, its relative power is low, and no noticeable fluctuations can be found in the streamlines or temperature field. Previously, the critical Rayleigh number Ra_c was discussed as the criterion for the onset time-dependent behaviour; however, it

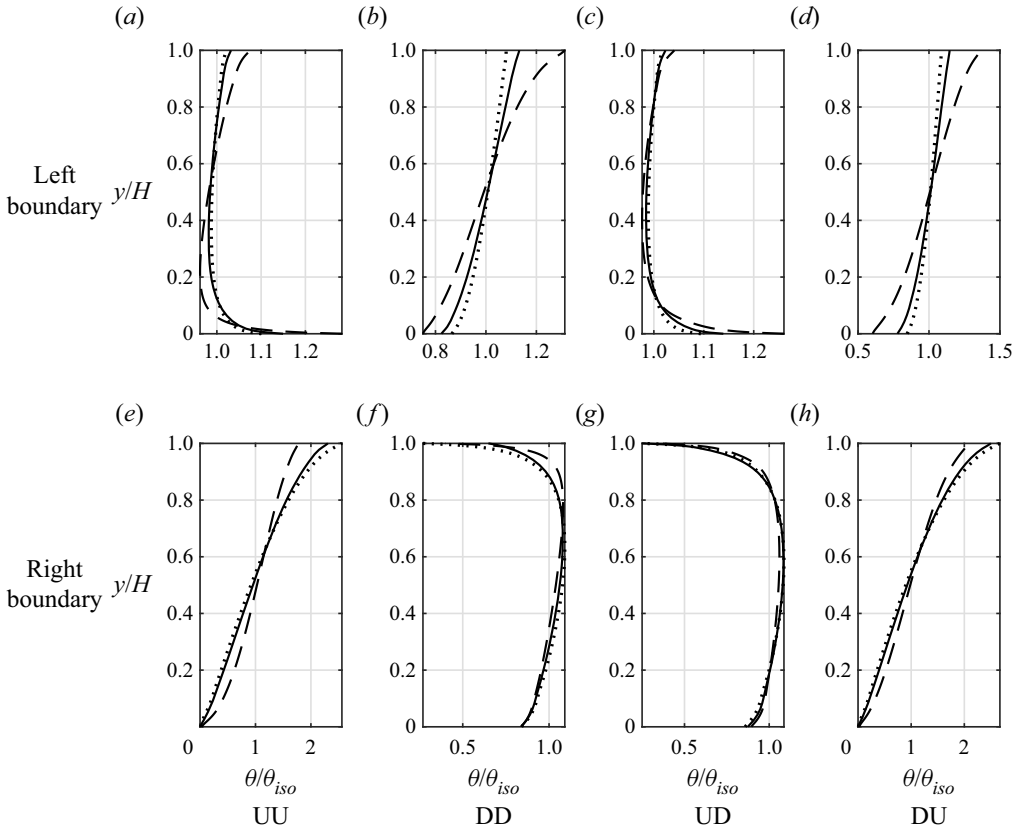

Figure 12. Wall temperature profiles for select CBC cases normalized by the mean wall temperature (wall temperature profile); (*a–d*) correspond to the left wall, and (*e–h*) correspond to the right wall. Solid line – $AR = 6$, $Re = 10^4$, $Ra = 2 \times 10^8$; Dashed line is for $AR = 6$,$Ra = 2 \times 10^8$ and different external Reynolds number case of $Re = 10^3$; and dotted line is associated with smaller aspect ratio of $AR = 4$, and $Re = 10^4$, $Ra = 2 \times 10^8$.

is clear that Ra alone cannot predict the transition to time dependence in cases with external CBCs.

The $AR = 4$ enclosure similarly exhibits the time-dependent mode ($\boldsymbol{\phi}_s$) with the UD configuration for $Re = 10^4$. The UU and DD configurations show time dependency, although they differ from those observed for the isothermal and UD boundary conditions. In figure 13, the time-dependent modes are shown for the case with $AR = 4$, $Ra = 2 \times 10^8$ and $Re = 10^4$ wherein the UU and DD cases introduce asymmetry to the flow and induce different time-dependent modes. The first dominant mode is similar to the previously observed time-dependent mode $\boldsymbol{\phi}_s$, but concentrated only at the ends of the enclosure. This can be seen in figure 13(*a–c*) where the latter 2 modes (*b*,*c*) split along the mid-height of the typical mode (*a*). These modes (*b*,*c*) have slightly different frequencies, $f_b = 0.028$ and $f_c = 0.026$, due to the difference in the mean free-stream velocity and the asymmetry of the corresponding external flow configurations.

In addition, a new time-dependent mode emerges, different from what has been observed in low ($\boldsymbol{\phi}_s$) and high ($\boldsymbol{\phi}_l$) aspect ratio cases. Figure 13(*d*) illustrates this new mode, which is a combination of the travelling wave mode in the boundary layer, and the mode associated with the impingement and separation at the end of the enclosures. This suggests that both

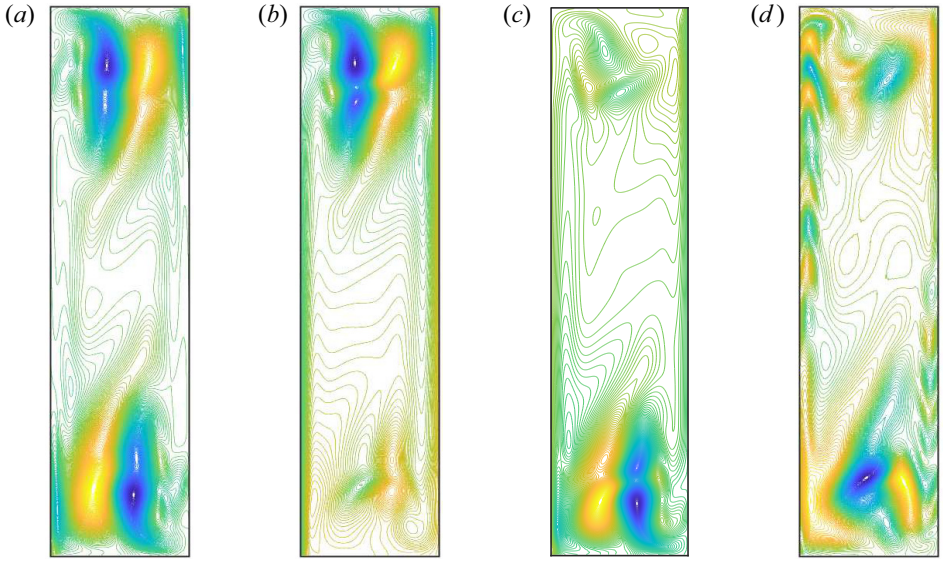

Figure 13. DMD modes for $AR = 4$ $Re = 10^4$ and $Ra = 2 \times 10^8$. (*a*) The dominant time-dependent mode (ϕ_s) for the UD configuration. (*b–d*) The 3 time-dependent modes present in the UU and DD configurations.

modes can be present independently or together in enclosures with $AR = 4$. A similar conclusion was made by Xin & Le Quéré (2006) regarding such intermediate aspect ratios.

Surprisingly, in the case of $AR = 2$, the effective Ra is always below the critical Rayleigh number, yet the time-dependent mode is still present for the UD configuration for the $Re = 10^4$ and $Ra = 2 \times 10^8$ case due to conjugate thermal boundary condition. It is evident that the UD configuration has a destabilizing effect on the system. Although the effective Ra is lower for the UD configuration than the other configurations, the fact that the UD cases always exhibit the time-dependent mode could translate into a more rapid transition to chaotic or turbulent flow at higher Ra. The DU configuration, on the other hand, can suppress the time-dependent modes even at supercritical Rayleigh numbers.

4. Conclusion

A numerical investigation and a reduced-order model of the flow and temperature of the natural convection inside a cavity with conjugate forced convection along the external side boundaries were presented. The effect of realistic thermal CBCs on the vertical sidewalls was investigated for different aspect ratios, internal Rayleigh number, external Reynolds number and external flow configurations. The average Nusselt number of sidewalls was explored to characterize the system's thermal performance. The isothermal boundary condition for each aspect ratio was compared with existing correlations and found to be in nearly perfect agreement with a minor modification of the temperature difference characteristic scale in the definition of the Rayleigh number. Modifying the definition of Ra with the appropriate characteristic temperature difference $\Delta T = T_H - 0.5(T_H + T_C)$, instead of the usual enclosure wall temperature difference, significantly improved the Nu predictions.

Furthermore, the flow dynamics was analysed by extracting the dynamic modes via DMD. A discrepancy was found for the time-dependent modes reported in the literature relative to the results presented here for $AR = 4$. It was observed that there are two

time-dependent modes for the DHC systems, small aspect ratios are associated with the low-frequency mode $\boldsymbol{\phi}_s$, and the large aspect ratios are associated with the high-frequency travelling wave mode $\boldsymbol{\phi}_l$. Previously, mode ϕ_s was observed in $AR \leq 3$ and mode ϕ_l in $AR \geq 4$, with multiple solutions existing between $3 < AR < 4$ at the critical Rayleigh number. Here, we showed that the mode ϕ_s is present in $AR \leq 4$. We note that the $AR = 4$ case with the low-frequency mode is at a supercritical Rayleigh number. However, the low-frequency mode $\boldsymbol{\phi}_s$ is associated with systems with detached flows at the end of the vertical boundary layers, which is the case for $AR = 4$ even at subcritical Rayleigh numbers.

The influence of the CBC on the thermal performance is characterized by the two boundary layers formed on either side of the vertical walls. The heat flux through the wall is limited by the thermal resistance of each of the boundary layers. Increasing the thermal resistance ratio, or equivalently increasing Re, enhances the heat transfer, and Nu approaches the isothermal boundary condition limit. For specific cases, when the ratio of the thermal resistances is unity, both boundary layers are of equal size. Furthermore, it was found that the DU configuration (counterflow) at the vertical walls has the highest heat transfer while the lowest heat transfer is associated with UD configuration (parallel flow). This is consistent with the theory and observation made in heat exchangers in which counterflow configurations always yield the highest heat transfer. The boundary-layer model initially proposed by Gill (1966) was modified to include the CBC. While capable of accurately predicting most cases of AR, Re, Ra and CBC configurations, it was shown that the model does not capture the response of cases affected by the separation region at the end walls. Besides these limited cases, the boundary-layer model provides a good estimation of Nu based on the Re, Ra and allows a relatively simple correlation for the heat transfer of these systems with or without CBC.

Comparing the CBC cases with the isothermal cases with equivalent Rayleigh numbers based on the vertical wall temperatures, Ra_{eff}, it is found that, while the average wall temperature difference at the wall is the same for both CBC and isothermal cases, the non-uniform temperature profile of the CBC cases serves to increase the overall heat transfer. This is especially true for the DU configuration and lower AR values.

The flow dynamics of the CBC configurations was also analysed using DMD. Although the time-dependent mode is present for $AR = 8$ and all CBC configurations, it is suppressed in smaller aspect ratios in all cases except the UD configuration. The $AR = 4$ enclosure, however, has a modified time-dependent mode due to the asymmetry introduced by the UU and DD configurations. The modified mode is similar to the original mode ϕ_s, but the top and bottom structures of the mode are at different frequencies. Surprisingly, for $AR = 2$, the effective Ra is always in the subcritical range, but the time-dependent mode is still present in the UD configuration. This leads us to believe that the wall temperature distribution of the UD configuration could result in an earlier transition to chaos/turbulence than would isothermal walls. In the future, the propagation of these effects at higher Ra should be studied to verify the transition to chaotic flow.

The results show that the main difference between low and large aspect ratios is principally due to flow instability. Large aspect ratios develop a shear instability in the boundary layer, while small aspect ratios have a separation region caused by the wall jet impingement. The mismatch between Nu prediction of the boundary-layer model and numerical calculations for $AR = 4$ is caused by this presence of the separation region as the nonlinear effect of the separation cannot be captured by the current boundary-layer model. This mismatch is almost not present in the isothermal case, where the thermal capacity of the system is reached before the separation region. The results align with previous

observations about the flow transition in the cavities with $3 < AR < 4$ and suggest that this aspect ratio can be used to enhance the heat transfer without the need for large external flow velocity on the side edge, while the thermal performance of these optimal cases can further improve with the right choice of external flow directions, DU configuration in the current set-up. It is interesting to extend the study to three-dimensional cavity configurations to determine to what extent the observed trends persist.

Acknowledgements. The authors would also like to acknowledge the Florida State University Research Computing Center and the NAVY DSRC for the computational resources on which these simulations were carried out.

Funding. This material is based upon research supported by, or in part by, the U.S. Office of Naval Research (ONR) under award number ONR N00014-16-1-2956 Electric Ship Research and Development Consortium; any opinions, findings, and conclusions or recommendations are those of the authors and do not necessarily reflect the views of ONR. The paper's control number is DCN 43-9373-22.

Declaration of interests. The authors report no conflict of interest.

Author ORCIDs.
Tomas Solano https://orcid.org/0000-0003-1885-9887;
Juan C. Ordonez https://orcid.org/0000-0002-3418-7091;
Kourosh Shoele https://orcid.org/0000-0003-2810-0065.

Appendix A

The following describes the boundary-layer model discussed in the main paper. The steps are similar to Gill (1966). However, for completeness, we present the derivation with the modified wall temperature condition. The equation for streamfunction, the conservation of momentum in vorticity form and the energy equation, all in dimensional form $(*)$ can be written as

$$\left.\begin{aligned} u^* = -\frac{\mathrm{d}\psi^*}{\mathrm{d}y^*} \quad \text{and} \quad v^* = \frac{\mathrm{d}\psi^*}{\mathrm{d}x^*} \\ u^*\frac{\mathrm{d}\omega^*}{\mathrm{d}x^*} + v\frac{\partial\omega^*}{\partial y^*} = \nu\left(\frac{\partial^2\omega^*}{\partial x^{*2}} + \frac{\partial^2\omega^*}{\partial y^{*2}}\right) + g\beta\frac{\partial T^*}{\partial x} \\ u^*\frac{\partial T^*}{\partial x^*} + v^*\frac{\partial T^*}{\partial y^*} = \alpha\left(\frac{\partial^2 T^*}{\partial x^{*2}} + \frac{\partial^2 T^*}{\partial y^{*2}}\right), \end{aligned}\right\} \tag{A1}$$

where the vorticity is

$$\omega^* = \frac{\partial^2\psi^*}{\partial x^{*2}} + \frac{\partial^2\psi^*}{\partial y^{*2}}. \tag{A2}$$

The boundary conditions are given as

$$\left.\begin{aligned} \psi^* = \frac{\partial\psi^*}{\partial x^*} = 0, \quad T^* = T_H \quad \text{at } x^* = 0, \\ \psi^* = \frac{\partial\psi^*}{\partial x^*} = 0, \quad T^* = T_C \quad \text{at } x^* = L, \\ \psi^* = \frac{\partial\psi^*}{\partial y^*} = 0, \quad \frac{\partial T^*}{\partial y^*} = 0 \quad \text{at } y^* = \pm\frac{1}{2}H. \end{aligned}\right\} \tag{A3}$$

Defining the following non-dimensional variables:

$$\left.\begin{gathered} x=\frac{x^*}{\delta}, \quad y=\frac{y^*}{H}, \quad T=\frac{T^*-\frac{1}{2}(T_H+T_C)}{\Delta T}, \quad \psi=\frac{\psi^*\delta}{\alpha H}, \\ u=\frac{\delta}{\alpha}u^*, \quad v=\frac{\delta^2}{\alpha H}v^*, \quad \omega=\frac{\delta^3}{\alpha H}\omega^*, \quad \delta=\frac{H}{Ra^{1/4}}, \end{gathered}\right\} \tag{A4}$$

where δ is the boundary-layer thickness, the boundary-layer equations can then be written in non-dimensional form as

$$\left.\begin{gathered} u=-\psi_y, \quad v=\psi_x \\ u\,T_x+v\,T_y=T_{xx} \\ \frac{1}{Pr}(u\omega_x+v\omega_y)=\omega_{xx}+T_x \\ \omega=\psi_{xx}=v_x, \end{gathered}\right\} \tag{A5}$$

and the boundary conditions at the wall are

$$\left.\begin{gathered} \psi=\psi_x=0, \quad T=T_w(y) \quad \text{at } x=0 \\ \psi=\psi_0(y), \quad T=T_0(y) \quad \text{at } x\to\infty \end{gathered}\right\}. \tag{A6}$$

As $x\to\infty$, the solution must match the core solution. This approximation is only valid if the length of the cavity L is much larger than the boundary layer δ or equivalently

$$\frac{L}{\delta}=\frac{L}{H}\left(\frac{Ra}{Pr}\right)^{1/4}\gg 1. \tag{A7}$$

The solutions of the flow and temperature fields near the vertical walls have been defined above by the boundary-layer problem. To deal with the nonlinearities of (A1), the Oseen linearization technique is used. The average value at each height $y=$ const., u_A and T'_A, are used as approximations in (A5). Integrating with respect to x results in the following relations for $Pr\to\infty$:

$$\left.\begin{gathered} u_A\,T_x+T'_A\,v=T_{xx}, \\ 0=w_{xx}+T-T_0. \end{gathered}\right\} \tag{A8}$$

Equations (A8) make up a system of the fourth order in x such that the solution may be written as

$$w=\sum_{n=1}^{4}a_n(y)\exp(\lambda_n(y)x), \tag{A9}$$

where $\lambda_n(y)$ are the roots of the quadratic equation $\lambda^3(\lambda+u_A)+T'_A=0$. This solution is valid for the whole boundary layer and the boundary conditions (A6) may then be applied to find w and θ

$$w=\frac{(T_w-T_0)}{(\lambda_2^2-\lambda_1^2)}\left(-\mathrm{e}^{-\lambda_2 x}+\mathrm{e}^{-\lambda_1 x}\right), \tag{A10}$$

$$\theta=T-T_0=\frac{(T_w-T_0)}{(\lambda_2^2-\lambda_1^2)}\left(\lambda_2^2\mathrm{e}^{-\lambda_2 x}-\lambda_1^2\mathrm{e}^{-\lambda_1 x}\right). \tag{A11}$$

To relate the average values of u_A and T'_A to the core values u_0 and T'_0, we use the von-Kármán–Polhausen integral method and define

$$\psi_0(y) = \int_0^\infty v \, \mathrm{d}x, \tag{A12}$$

$$\frac{\partial}{\partial y}\int_0^\infty v\theta \, \mathrm{d}x + \psi_0 T'_0 = -\left.\frac{\partial \theta}{\partial x}\right|_{x=0}. \tag{A13}$$

Substituting (A10) and (A11) into (A12) and (A13) results in

$$\psi_0 = \frac{T_w - T_0}{\lambda_1\lambda_2(\lambda_1+\lambda_2)}, \tag{A14}$$

$$\frac{\mathrm{d}}{\mathrm{d}y}\left(\frac{(T_w-T_0)^2}{(2(\lambda_1+\lambda_2)^3)}\right) + \psi_0 T'_0 = (T_w - T_0)\frac{\lambda_1+\lambda_2-(\lambda_1\lambda_2)}{\lambda_1+\lambda_2}. \tag{A15}$$

Moreover, since the solution should be dependent only on the invariants $\tau = \lambda_1 + \lambda_2$ and $\chi = \lambda_1\lambda_2$, we can rewrite it as

$$\frac{\mathrm{d}}{\mathrm{d}y}\left(\frac{(T_w-T_0)^2}{(2\tau^3)}\right) + \psi_0 T'_0 = (T_w - T_0)\left(\tau - \frac{\chi}{\tau}\right), \tag{A16}$$

and with the use of (A14),

$$\frac{4\tau(T_w-T_0)(T'_w-T'_0) - 6(T_w-T_0)^2\tau'}{4\tau^4} + \frac{(T_w-T_0)}{\tau\chi}T'_0 = (T_w-T_0)\left(\tau - \frac{\chi}{\tau}\right). \tag{A17}$$

Note u_A and T_H are odd functions of y, therefore the four roots are $\lambda_1(y)$, $\lambda_2(y)$, $-\lambda_1(-y)$, $-\lambda_2(-y)$. Using these in the fourth-order polynomial for the roots, we can write the following relations:

$$\left.\begin{aligned} \tau(-y) - \tau(y) &= u_A, \\ \chi(y) + \chi(-y) &= \tau(y)\tau(-y), \\ \tau(y)\chi(-y) &= \tau(-y)\chi(y), \\ \chi(y)\chi(-y) &= T_A. \end{aligned}\right\} \tag{A18}$$

Next, the invariants can be recast in terms of odd and even functions q, and v. The condition that u_0, T_0, u_A, T_H are odd functions of y can be used to simplify the equation. Here, the even function is defined by

$$h = \tau(-y) + \tau(y), \tag{A19}$$

and the odd function by

$$p = u_A/h, \tag{A20}$$

to express the solutions of τ and χ as

$$\left.\begin{aligned} \tau &= \tfrac{1}{2}h(1-p), \\ \chi &= \tfrac{1}{8}h^2(1-p^2)(1-p), \\ \lambda_{1,2} &= \tfrac{1}{4}h(1-p)[1 \pm \mathrm{i}\sqrt{1+2p}]. \end{aligned}\right\} \tag{A21}$$

Equations (A21) and (A14) provide the solution for T_0 and ψ_0. In particular, since ψ_0 is an even function of y, the odd part must be zero, and T_0 can be expressed as

$$T_0 = \frac{1}{2}\left(T_w(y) - T_w(-y)\right) + \frac{q}{1+q^2}\left(T_w(y) + T_w(-y)\right). \tag{A22}$$

Similarly, the solution for ψ_0 is given as

$$\psi_0 = \frac{8(T_w(y) + T_w(-y))}{h^3(1-p^4)}. \tag{A23}$$

Finally, we can rewrite (A17) using the T_0 expression as

$$[7-4p+3p^2](T_w+\bar{T}_w)p' - \frac{3(T_w+\bar{T}_w)(1-p)(1+p^2)}{h}h' - \frac{1}{8}h^4(1-p)^4(1+p^2)^2 + \left(\frac{(2(1+p^2)(3+p^2))}{(1-p)}\right)T_w' - \left(\frac{2(1+p^2)(1-p)^3}{(1-p^2)}\right)\bar{T}_w' = 0, \tag{A24}$$

where $\bar{T}_w = T_w(-y)$ and $\bar{T}_w' = T_w'(-y)$. This is the governing equation for the boundary layer on the left wall of the enclosure. The same equation can be written for the right side of the enclosure. However, due to the centrosymmetric property of the system., we can solve for the even and odd parts of (A24). The odd part being

$$-8(T_w+\bar{T}_w)pp' - \frac{6(T_w+\bar{T}_w)(1+p^2)}{h}h' + ph^4(1+p^2)^3 + \frac{4(1+p^2)(2+p+p^2)}{(1-p)}T_w' - \frac{4(1+p^2)(2-p+p^2)}{(1+p)}T_w' = 0 \tag{A25}$$

and the even part

$$(14+6p^2)(T_w+\bar{T}_w)p' + \frac{6p(T_w+\bar{T}_w)(1+p^2)}{h}h' - \frac{1}{4}h^4(1+p^2)^2(1+6p^2+p^4) + 4(1+p^2)T_w' = 0. \tag{A26}$$

The two coupled differential equations involve p, h, T_w and their derivatives with respect to y and are subject to the boundary conditions

$$\int_0^L \rho c v^* T^* - k\frac{\mathrm{d}T^*}{\mathrm{d}y^*}\mathrm{d}x^* = 0 \quad \text{at } y^* = \pm\frac{H}{2}. \tag{A27}$$

This is equivalent to imposing a zero heat flux condition at the top and bottom of the enclosure as proposed by Bejan (1979). Re-writing in our non-dimensional variables

$$\frac{L}{\delta}\int_0^{L/\delta} vT\,\mathrm{d}x - \frac{L\delta}{H}\int_0^{L/\delta}\frac{\mathrm{d}T}{\mathrm{d}y}\mathrm{d}x = 0 \quad \text{at } y = \pm\frac{H}{2}, \tag{A28}$$

where $\delta = HRa^{-1/4}$ is the boundary-layer thickness. The first term of (A28) is for the convective effects and the second the conduction effects. The differential equations along with the boundary conditions can be solved as long as the temperature distribution at the wall (T_w) is known.

References

Abourida, B., Hasnaoui, M. & Douamna, S. 1999 Transient natural convection in a square enclosure with horizontal walls submitted to periodic temperatures. *Numer. Heat Tr. A: Appl.* **36** (7), 737–750.

Anderson, R. & Bejan, A. 1980 Natural convection on both sides of a vertical wall separating fluids at different temperatures. *Trans. ASME J. Heat Transfer* **102**, 630–631.

Armenio, V. & Sarkar, S. 2002 An investigation of stably stratified turbulent channel flow using large-eddy simulation. *J. Fluid Mech.* **459**, 1–42.

Asgarian, A., Hossain, M.Z. & Floryan, J.M. 2016 Rayleigh–Bénard convection driven by a long wavelength heating. *Theor. Comput. Fluid Dyn.* **30** (4), 313–337.

Azzoune, M., Mammou, L., Boulheouchat, M.H., Zidi, T., Mokeddem, M.Y., Belaid, S., Salah, A.B., Meftah, B. & Boumedien, A. 2010 NUR research reactor safety analysis study for long time natural convection (NC) operation mode. *Nucl. Engng Des.* **240** (4), 823–831.

Batchelor, G.K. 1954 Heat transfer by free convection across a closed cavity between vertical boundaries at different temperatures. *Q. Appl. Maths* **12** (3), 209–233.

Bejan, A. 1979 Note on Gill's solution for free convection in a vertical enclosure. *J. Fluid Mech.* **90** (3), 561–568.

Bejan, A. 2013 *Convection Heat Transfer*. John Wiley & Sons.

Buchberg, H., Catton, I. & Edwards, D.K. 1976 Natural convection in enclosed spaces: a review of application to solar energy collection. *Trans. ASME J. Heat Transfer* **98** (2), 182–188.

Çengel, Y.A., Turner, R.H., Cimbala, J.M. & Kanoglu, M. 2008 *Fundamentals of Thermal-Fluid Sciences*, vol. 703. McGraw-Hill.

Chorin, P., Moreau, F. & Saury, D. 2018 Heat transfer modification induced by a localized thermal disturbance in a differentially-heated cavity. *Intl J. Therm. Sci.* **125**, 101–110.

Christon, M.A., Gresho, P.M. & Sutton, S.B. 2002 MIT special issue on thermal convection. Issue edited by Mark A. Christon. *Intl J. Numer. Meth. Fluids* **40** (8), 953–980.

De Vahl Davis, G. 1983 Natural convection of air in a square cavity: a bench mark numerical solution. *Intl J. Numer. Meth. Fluids* **3** (3), 249–264.

El Sherbiny, S.M., Raithby, G.D. & Hollands, K.G.T. 1982 Heat transfer by natural convection across vertical and inclined air layers. *Trans. ASME J. Heat Transfer* **104** (1), 96–102.

Floryan, J.M., Shadman, S. & Hossain, M.Z. 2018 Heating-induced drag reduction in relative movement of parallel plates. *Phys. Rev. Fluids* **3** (9), 094101.

Ganguli, A.A., Pandit, A.B. & Joshi, J.B. 2009 CFD simulation of heat transfer in a two-dimensional vertical enclosure. *Chem. Engng Res. Des.* **87** (5), 711–727.

Gill, A.E. 1966 The boundary-layer regime for convection in a rectangular cavity. *J. Fluid Mech.* **26** (3), 515–536.

Hasan, N. & Sanghi, S. 2007 Proper orthogonal decomposition and low-dimensional modelling of thermally driven two-dimensional flow in a horizontal rotating cylinder. *J. Fluid Mech.* **573**, 265–295.

Howle, L.E. 1997 Active control of Rayleigh–Bénard convection. *Phys. Fluids* **9** (7), 1861–1863.

Kakac, S., Liu, H. & Pramuanjaroenkij, A. 2002 *Heat Exchangers: Selection, Rating, and Thermal Design*. CRC.

Kays, W.M. & Alexander, L.L. 1998 *Compact Heat Exchangers*. Krieger.

Kim, B.S., Lee, D.S., Ha, M.Y. & Yoon, H.S. 2008 A numerical study of natural convection in a square enclosure with a circular cylinder at different vertical locations. *Intl J. Heat Mass Transfer* **51** (7–8), 1888–1906.

Kwak, H.S. & Hyun, J.M. 1996 Natural convection in an enclosure having a vertical sidewall with time-varying temperature. *J. Fluid Mech.* **329**, 65–88.

Kwak, H.S., Kuwahara, K. & Hyun, J.M. 1998 Resonant enhancement of natural convection heat transfer in a square enclosure. *Intl J. Heat Mass Transfer* **41** (18), 2837–2846.

Lage, J.L. & Bejan, A. 1993 The resonance of natural convection in an enclosure heated periodically from the side. *Intl J. Heat Mass Transfer* **36** (8), 2027–2038.

Lappa, M. 2016 Control of convection patterning and intensity in shallow cavities by harmonic vibrations. *Microgravity Sci. Technol.* **28** (1), 29–39.

Le Quéré, P. 1990 A note on multiple and unsteady solutions in two-dimensional convection in a tall cavity. *Trans. ASME J. Heat Transfer* **112** (4), 965–974.

Le Quéré, P. 1991 Accurate solutions to the square thermally driven cavity at high Rayleigh number. *Comput. Fluids* **20** (1), 29–41.

Lumley, J.L. & Poje, A. 1997 Low-dimensional models for flows with density fluctuations. *Phys. Fluids* **9** (7), 2023–2031.

MARELLA, S., KRISHNAN, S.L.H.H., LIU, H. & UDAYKUMAR, H.S. 2005 Sharp interface Cartesian grid method I: an easily implemented technique for 3D moving boundary computations. *J. Comput. Phys.* **210** (1), 1–31.

NG, C.S., OOI, A., LOHSE, D. & CHUNG, D. 2015 Vertical natural convection: application of the unifying theory of thermal convection. *J. Fluid Mech.* **764**, 349–361.

OJO, O. & SHOELE, K. 2021 Load reduction and reconfiguration capabilities of branched trees. In *Integrative and Comparative Biology*, vol. 61, pp. E664–E664. Oxford University Press Inc.

ORTEGA, A. & RAMANATHAN, S. 2003 On the use of point source solutions for forced air cooling of electronic components–part I: thermal wake models for rectangular heat sources. *J. Electron. Packaging* **125** (2), 226–234.

OSTRACH, S. 1972 Natural convection in enclosures. In *Advances in Heat Transfer*, vol. 8, pp. 161–227. Elsevier.

PAOLUCCI, S. & CHENOWETH, D.R. 1989 Transition to chaos in a differentially heated vertical cavity. *J. Fluid Mech.* **201** (1), 379–410.

PENOT, F., SKURTYS, O. & SAURY, D. 2010 Preliminary experiments on the control of natural convection in differentially-heated cavities. *Intl J. Therm. Sci.* **49** (10), 1911–1919.

PURAGLIESI, R. & LERICHE, E. 2012 Proper orthogonal decomposition of a fully confined cubical differentially heated cavity flow at Rayleigh number $Ra = 109$. *Comput. Fluids* **61**, 14–20.

RAMOS, E.M., DO NASCIMENTO, F., DARZE, G.M., FACCINI, J.L.H. & GIRALDI, G.A. 2019 Dynamic mode decomposition of numerical data in natural circulation. *Braz. J. Radiat. Sci.* **8** (3A), 18.

RHIE, C.M. & CHOW, W.-L. 1983 Numerical study of the turbulent flow past an airfoil with trailing edge separation. *AIAA J.* **21** (11), 1525–1532.

RIPS, A., SHOELE, K. & MITTAL, R. 2020 Heat transfer enhancement in laminar flow heat exchangers due to flapping flags. *Phys. Fluids* **32** (6), 063603.

SALVETTI, M.V., ZANG, Y., STREET, R.L. & BANERJEE, S. 1997 Large-eddy simulation of free-surface decaying turbulence with dynamic subgrid-scale models. *Phys. Fluids* **9** (8), 2405–2419.

SCHEEL, J.D. & SCHUMACHER, J. 2014 Local boundary layer scales in turbulent Rayleigh–Bénard convection. *J. Fluid Mech.* **758**, 344–373.

SCHMID, P.J. 2010 Dynamic mode decomposition of numerical and experimental data. *J. Fluid Mech.* **656**, 5–28.

SHAH, R.K. & SEKULIC, D.P. 2003 *Fundamentals of Heat Exchanger Design*. John Wiley & Sons.

SHOELE, K. & MITTAL, R. 2014 Computational study of flow-induced vibration of a reed in a channel and effect on convective heat transfer. *Phys. Fluids* **26** (12), 127103.

SHU, J.J. & POP, I. 1999 Thermal interaction between free convection and forced convection along a vertical conducting wall. *Heat Mass Transfer* **35** (1), 33–38.

TAIRA, K., BRUNTON, S.L., DAWSON, S.T.M., ROWLEY, C.W., COLONIUS, T., MCKEON, B.J., SCHMIDT, O.T., GORDEYEV, S., THEOFILIS, V. & UKEILEY, L.S. 2017 Modal analysis of fluid flows: an overview. *AIAA J.* **55** (12), 4013–4041.

THIERS, N., GERS, R. & SKURTYS, O. 2020 Heat transfer enhancement by localised time varying thermal perturbations at hot and cold walls in a rectangular differentially heated cavity. *Intl J. Therm. Sci.* **151**, 106245.

TREVIÑO, C., MENDEZ, F. & HIGUERA, F.J. 1996 Heat transfer across a vertical wall separating two fluids at different temperatures. *Intl J. Heat Mass Transfer* **39** (11), 2231–2241.

TURAN, O., POOLE, R.J. & CHAKRABORTY, N. 2012 Influences of boundary conditions on laminar natural convection in rectangular enclosures with differentially heated side walls. *Intl J. Heat Fluid Flow* **33** (1), 131–146.

VIJAYSHANKAR, S., NABI, S., CHAKRABARTY, A., GROVER, P. & BENOSMAN, M. 2020 Dynamic mode decomposition and robust estimation: case study of a 2D turbulent Boussinesq flow. In *2020 American Control Conference (ACC)*, pp. 2351–2356. IEEE.

WAN, D.C., PATNAIK, B.S.V. & WEI, G.W. 2001 A new benchmark quality solution for the buoyancy-driven cavity by discrete singular convolution. *Numer. Heat Tr. B: Fund.* **40** (3), 199–228.

XIN, S. & LE QUÉRÉ, P. 2006 Natural-convection flows in air-filled, differentially heated cavities with adiabatic horizontal walls. *Numer. Heat Tr. A: Appl.* **50** (5), 437–466.

XU, F. 2006 Transient natural convection in a differentially heated cavity with and without a fin on the sidewall. PhD thesis, James Cook University.

YANG, S., PILET, T.J. & ORDONEZ, J.C. 2018 Volume element model for 3D dynamic building thermal modeling and simulation. *Energy* **148**, 642–661.

YANG, S. & ORDONEZ, J.C. 2019 Optimal cooling channel layout in a hot enclosure subject to natural convection. *Trans. ASME J. Heat Transfer* **141** (11), 112502.

YE, T., MITTAL, R., UDAYKUMAR, H.S. & SHYY, W. 1999 An accurate Cartesian grid method for viscous incompressible flows with complex immersed boundaries. *J. Comput. Phys.* **156** (2), 209–240.

YUAN, L.L., STREET, R.L. & FERZIGER, J.H. 1999 Large-eddy simulations of a round jet in crossflow. *J. Fluid Mech.* **379**, 71–104.

YUCEL, N. & TURKOGLU, H. 1998 Numerical analysis of laminar natural convection in enclosures with fins attached to an active wall. *Heat Mass Transfer* **33** (4), 307–314.

ZANG, Y., STREET, R.L. & KOSEFF, J.R. 1994 A non-staggered grid, fractional step method for time-dependent incompressible Navier–Stokes equations in curvilinear coordinates. *J. Comput. Phys.* **114** (1), 18–33.

ZHOU, Q., STEVENS, R.J.A.M., SUGIYAMA, K., GROSSMANN, S., LOHSE, D. & XIA, K.Q. 2010 Prandtl–Blasius temperature and velocity boundary-layer profiles in turbulent Rayleigh–Bénard convection. *J. Fluid Mech.* **664**, 297–312.

ZHOU, Q. & XIA, K.Q. 2010 Measured instantaneous viscous boundary layer in turbulent Rayleigh–Bénard convection. *Phys. Rev. Lett.* **104** (10), 104301.